Resonant multiwave-mixing spectra of gas-phase sodium: Nonperturbative calculations

Robert P. Lucht, Rick Trebino, and Larry A. Rahn
Combustion Research Facility, Sandia National Laboratories, Livermore, California 94551
(Received 12 August 1991)

We perform nonperturbative calculations of resonant multiwave mixing of two high-intensity laser beams of different frequencies both for a general three-level system and for the $3\,^2S_{1/2}-3\,^2P_{1/2}$ electronic resonance of the sodium atom. Our calculations proceed by direct numerical integration of the density-matrix equations and subsequent Fourier analysis of the calculated time-dependent density-matrix elements. We examine the case where two nearly degenerate input beams are each detuned many collisional linewidths from electronic resonance, and the frequency difference between the input beams is tuned through a ground-state resonance. Unlike previous high-intensity analyses, each input beam can be resonant with numerous transitions simultaneously; for a three-level system, we refer to this as an "M-type" system, in analogy with Λ- and V-type systems. Calculated four-, six-, and eight-wave-mixing spectra exhibit subharmonic resonances of the type observed experimentally by Trebino and Rahn [Opt. Lett. **12**, 912 (1987)]. The three-level system is studied to gain insight into the physics of these subharmonic resonances. For more quantitative comparison with experiment, we use a model that includes the 16 Zeeman and hyperfine states in the $3\,^2S_{1/2}$ and the $3\,^2P_{1/2}$ levels, and accounts for arbitrary linear polarization of the input laser radiation. The relative intensities of the resonance features in the calculated multiwave-mixing spectra show good agreement with experiment. These resonance features broaden and shift as laser intensity increases, as predicted for four-wave-mixing processes in previous, less general high-intensity analyses. Both theory and experiment also show additional resonant features in the eight-wave-mixing spectra that appear at very high intensity.

PACS number(s): 42.65.−k, 32.80.−t, 31.30.Gs, 02.60.+y

I. INTRODUCTION

The physics of wave-mixing interactions has been the subject of intense research activity for the past few decades. Much of this work, both experimental and theoretical, has been based on perturbation theory, which suffices for most low-intensity cases. The second- and third-order susceptibilities, for example, form the basis of many important diagnostic methods and optical devices. Phase conjugation, harmonic generation, frequency shifting of laser radiation, and various laser methods for probing the spectroscopy and thermodynamic properties of media [1–5] are just a few techniques that have been successfully described by theories that are perturbative with respect to the interaction of laser radiation with electronic resonances. For example, coherent anti-Stokes Raman scattering (CARS) is a well-developed four-wave-mixing technique for measuring temperature and detection of gas-phase species [3-5]. For diagnostic applications of CARS, laser intensities are typically limited so that the third-order susceptibility given by perturbation theory is still valid (i.e., negligible population transfer and Stark shifting).

Higher-order wave-mixing effects have been observed in several experiments. Zhang, Wang, and Schawlow [6] and Zhang and Schawlow [7] studied the generation of coherent ultraviolet radiation by four- and six-wave mixing in gas-phase potassium. Reintjes, She, and Eckardt [8] observed frequency conversion of 266-nm laser radiation in helium due to $\chi^{(5)}$ and $\chi^{(7)}$ processes. In this investigation some care was required to determine that frequency conversion was due to true $\chi^{(5)}$ and $\chi^{(7)}$ processes and not to cascade generation of higher harmonics by multiple lower-order wave-mixing processes. Raj *et al.*, [9] used higher-order phase-matching geometries to study higher-order susceptibilities in resonant, degenerate wave mixing. Trebino and Rahn [10] observed effects due to nonlinear susceptibilities as high order as $\chi^{(13)}$ in an eight-wave-mixing geometry in nearly degenerate wave mixing in gas-phase sodium in a flame. Debarre, Lefebvre, and Pealat [11] observed six-wave-mixing effects in vibrational CARS spectroscopy of hydrogen and nitrogen, where the pump and Stokes laser frequencies were far from electronic resonance. Higher-order wave-mixing effects were probably also observed by Zheng, Wang, and Wu [12], who postulated that higher-order wave mixing was responsible for sidebands in the output of a bifrequency HeNe Zeeman laser. Very-high-order wave mixing has been observed in the interaction of very-high-intensity laser radiation with noble-gas atoms; harmonics of order 31 and higher have been observed [13,14]. These effects involve very high laser intensities, on the order of 10^{13} W/cm^2, where perturbation theory ceases to be valid and significant Stark shifting and photoionization occur. Kulander and Shore [15] and Eberly, Su, and Javanainen [16] have successfully modeled this process by direct numerical integration of the time-dependent Schrödinger wave equation.

The theoretical work discussed in this paper was motivated by the experiments of Trebino and Rahn [10] who observed higher-order effects in the course of performing four-wave mixing (4WM) experiments on sodium

in flames. In their experiments, two pulsed, nearly Fourier-transform-limited laser beams with frequencies ω_1 and ω_2 approximately 2 cm^{-1} below the $3\,^2S_{1/2}$–$3\,^2P_{1/2}$ electronic resonance were used to excite the sodium atom. The energy-level diagram for the 4WM experiment is shown in Fig. 1. Spectra for this system were determined as a function of detuning frequency $\omega_1-\omega_2$; ω_1 was fixed and ω_2 scanned across the hyperfine resonances. At low laser intensities, in the absence of a magnetic field, 4WM resonances were observed at $\omega_1-\omega_2=0$, corresponding to the Zeeman coherence, and at

$$\omega_1-\omega_2=\pm 0.059\ cm^{-1}\ , \tag{1}$$

corresponding to the hyperfine splitting ω_{hfs}.

The effect of collisions and the laser polarizations on these resonances had been investigated previously in detail by Rothberg and Bloembergen [17] using cw lasers in a sodium cell. The experiments of Trebino and Rahn were performed at much higher laser intensities than those of Rothberg and Bloembergen. At low laser intensities, the spectra of Trebino and Rahn were qualitatively similar to those of Rothberg and Bloembergen. As laser intensities increased, however, the 4WM resonances at ω_{hfs} broadened and, more significantly, spectral features appeared at the subharmonic resonance frequency $\omega_{hfs}/2$. Hypothesizing that these subharmonic resonances were the result of higher-order wave-mixing processes, Trebino and Rahn performed experiments using higher-order phase-matching schemes to selectively detect signals due to six- and eight-wave mixing. A typical eight-wave-mixing spectrum is shown in Fig. 2. Strong subharmonic

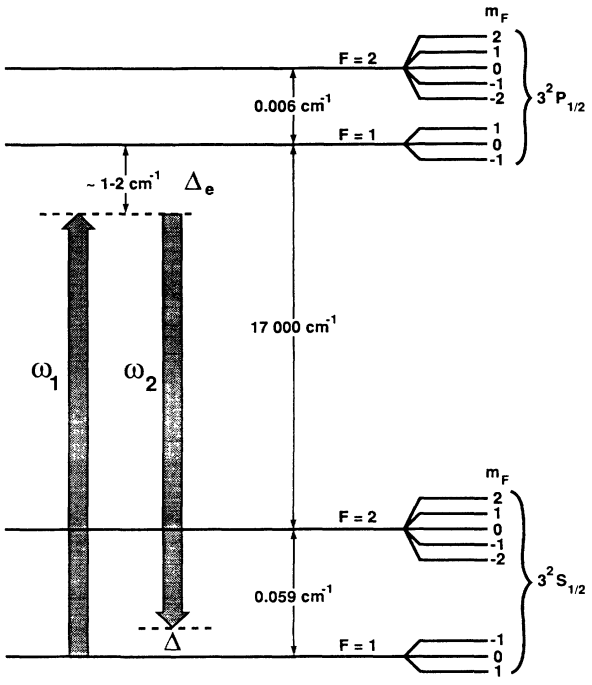

FIG. 1. Energy-level diagram for multiwave mixing in the sodium $3\,^2S_{1/2}$–$3\,^2P_{1/2}$ electronic system.

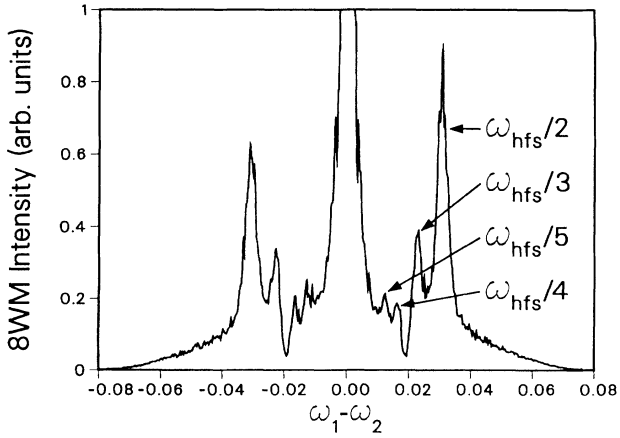

FIG. 2. Eight-wave-mixing spectrum for gas-phase sodium in a flame [10].

resonances are observed at $\pm\omega_{hfs}/2$ and $\pm\omega_{hfs}/3$; weaker subharmonic resonances are also apparent at $\pm\omega_{hfs}/4$ and $\pm\omega_{hfs}/5$.

Perturbation theory has been very useful in describing these higher-order wave-mixing experiments. Agarwal [18] used perturbation theory (and several other approaches) to derive the existence and frequencies of subharmonic resonances seen in several higher-order experiments. Kothari and Agarwal [19] considered the effects of collisional mixing on subharmonics that overlap in molecular spectra using the fifth-order susceptibility. Trebino and Rahn [20] used perturbation theory to explain the subharmonics they saw at $\frac{1}{2}$, $\frac{1}{3}$, $\frac{1}{4}$, and $\frac{1}{5}$ of the hyperfine splitting ω_{hfs} of the sodium ground state. Indeed, their theoretical eight-wave-mixing spectrum fits their data reasonably well, except near zero frequency, where contributions from twelve-wave and higher-order wave mixing are probably important. The advantage of perturbation theory is that simple energy-level diagrams or Feynman diagrams show that subharmonics at $1/n$ of a transition frequency result simply from $2n$-photon resonances; the resulting resonance condition is

$$(\omega_1-\omega_2)=\omega_{hfs}/n\ . \tag{2}$$

While the simple explanation of the existence of subharmonic resonances that is provided by perturbation theory is encouraging, there are severe drawbacks to its use in general for describing these experiments. As was apparent in the experiment of Trebino and Rahn [10], the range of applicability of perturbation theory can be quite small for a higher-order wave-mixing experiment: Shortly after sufficient intensity is attained to generate significant signal from a higher-order effect, still higher-order processes must be considered. Consequently, perturbation-theory calculations can be become quite intractable, and it becomes difficult to extract understanding of the underlying physical processes involved in higher-order wave mixing, thus eliminating one of the major advantages of the use of perturbation theory. In addition, because monochromatic laser radiation is gen-

erally assumed in frequency-domain perturbation theory, a frequency convolution over laser line shapes must be performed, and this convolution is very complex for higher-order wave mixing, involving many different integrals for a given resonance. Worse, the applicability of some of the major assumptions of the perturbation approach is questionable for modeling these high-intensity experimental spectra. In particular, the assumptions of negligible population transfer and steady state probably did not hold for any but the lowest laser intensities used by Trebino and Rahn [10].

Various approaches, such as transformations to rotating frames or the use of dressed states, have traditionally been used to describe high-intensity problems. Such approaches to nonlinear-optical wave mixing have been succinctly reviewed by Levine *et al.* [21]. We mention a few important examples of this work here. Levine *et al.* [21] solved the Maxwell-Bloch equations for four-wave mixing in a four-level system analytically, assuming that each of the three laser fields considered interacted only with a single pair of levels and that there was no collisional or radiative damping. In a later article by the same group, Chencinski *et al.* [22] included collisional and/or radiative relaxation in their treatment of the problem. Dick and Hochstrasser [23] also considered four-wave mixing in a four-level system. They included damping in their treatment, but assumed that one field was weak and obtained a perturbation-theory solution to the problem. Wilson-Gordon and Friedmann [24] considered saturation effects in four-wave-mixing spectra in a two-level system where one of the beams was nearly resonant and the other beam was tuned through electronic resonance.

While this work has resulted in the elucidation of the fundamental physics of the four-wave-mixing interaction of high-intensity laser radiation in simple systems, more complex interactions with many-level systems (e.g., actual atoms and molecules) have not received much attention. In addition, it has generally been assumed that each input beam can be resonant with only one transition. In real systems, by contrast, degeneracies abound, and each laser beam may be nearly resonant with several transitions with nonzero dipole-moment matrix elements. None of the above work considered the possibility of higher-order wave mixing.

Agarwal [25] developed a nonperturbative model for higher-order wave mixing in an idealized three-level system (lower levels a and b, upper level c). Using an effective Hamiltonian that couples the Stokes and anti-Stokes lines, he was able to derive the odd subharmonics. He calculated the two-beam-coupling gain, the four-wave-mixing signal, and the six-wave-mixing signal. At high intensity, he obtained broadening and frequency shifts of these new resonances (to larger values of $\omega_1-\omega_2$) in all spectra. In addition to a deep hole appearing in the two-photon resonance line of the four-wave-mixing spectrum, as seen in other four-wave-mixing work, he saw a small dip in the $\omega_{ab}/3$ resonance line at high intensity. Oliveira *et al.* [26] have considered theoretically six-wave mixing in a four-level system (lower levels a and b, upper levels c and d), assuming that the laser beam at ω_1 is resonant with electronic transition ac. They predict Stark splittings in the six-wave-mixing spectrum as ω_2 is tuned, corresponding to the Rabi frequency for the interaction of the laser field at ω_1 with the resonance ac. While these studies are very interesting, it is not possible to compare the results with experiment because only idealized three- and four-level systems were considered.

In this paper we model the resonant higher-order wave-mixing spectra of Trebino and Rahn [10] using a nonperturbative approach involving direct numerical integration of the density-matrix equations. In our analysis, the time-dependent density-matrix equations are solved for a multilevel system irradiated by two nearly resonant, nearly frequency-degenerate laser beams. This approach is similar to previous studies of saturation in CARS (Refs. [27–29]) and of picosecond-pulse amplification in a multilevel XeCl excimer gain medium [30]. The assumptions of steady state and negligible population transfer are unnecessary with this approach. In addition, because the laser temporal pulse shape is a direct input to the code and the time-dependent medium polarization is calculated directly, no frequency convolutions are necessary in the calculation of the multiwave-mixing spectra. We allow all input beams to be resonant with all (electronic) transitions. In analogy with Λ- and V-type systems, we call this an "M-type" system in the limit of three levels. The reason for this name is evident in Fig. 3.

We compute spectra, both for a three-level system and for the hyperfine and Zeeman-level system of sodium, showing the wave-mixing signal strength versus frequency difference in four-, six-, and eight-wave beam geometries. At low intensities, we find that subharmonics appear in the higher-order spectra (unless prohibited by selection rules). At higher intensities, additional subharmonics appear at lower frequency $\omega_{\rm hfs}/n$, where n increases. These results are as expected from perturbation theory. At higher intensities, however, effects generally associated with the breakdown of perturbation theory occur, such as spectral-line broadening and shifting. The magnitudes and directions of the shifts vary from subharmonic to subharmonic. The relative intensities of the subharmonic spectral features change significantly as laser intensity increases; at higher intensities, high-order subharmonics grow to dominate the lower-order subharmonics. At the highest intensities considered, a dip appears in one of the subharmonic resonances, drifting across the spectral line as laser intensity increases. In ad-

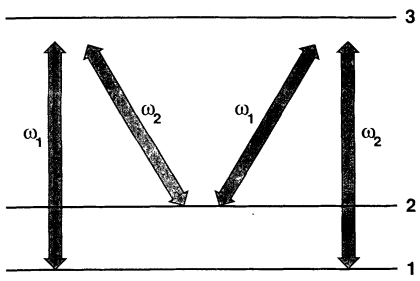

FIG. 3. Schematic diagram of the M-type system.

dition, resonances of unknown origin appear at these high laser intensities.

II. DENSITY-MATRIX FORMULATION FOR CALCULATION OF MULTIWAVE-MIXING SPECTRA

A. Manipulation of the density-matrix equations for computer solution

The interaction of laser radiation with a multilevel system is described by the time-dependent density-matrix equations [31–33]

$$\dot{\rho}_{kk}=-\frac{i}{\hbar}\sum_m (V_{km}\rho_{mk}-\rho_{km}V_{mk})-\Gamma_k\rho_{kk}+\sum_m \Gamma_{mk}\rho_{mm} , \tag{3}$$

$$\dot{\rho}_{kj}=-\rho_{kj}(i\omega_{kj}+\gamma_{kj})-\frac{i}{\hbar}\sum_m (V_{km}\rho_{mj}-\rho_{km}V_{mj}) , \tag{4}$$

where j, k, and m are arbitrary levels. For the off-diagonal matrix elements, $\rho_{kj}=\rho_{jk}^*$. The angular frequency $\omega_{kj}=(W_k-W_j)/\hbar$, where W_k is the energy of level k. The quantity γ_{kj} is the dephasing-rate constant for the off-diagonal matrix element ρ_{kj}. The quantity Γ_{kj} is the sum of the spontaneous-emission and collisional-transfer-rate constants from level k to level j, and Γ_k is the total transfer-rate constant out of level k.

The interaction matrix element V_{km} is given by

$$V_{km}=-\mathbf{d}_{km}\cdot\mathbf{E}(t) , \tag{5}$$

where $\mathbf{d}_{km}$ is the electric dipole matrix element and $\mathbf{E}(t)$ is the electric field. The dipole matrix elements $\mathbf{d}_{kk}=0$. When k and m are both upper or both lower levels, $\mathbf{d}_{km}=0$. The electric field is given by

$$\mathbf{E}(t)=\tfrac{1}{2}\{\hat{\mathbf{e}}_1 A_1(t)\exp[i(\mathbf{k}_1\cdot\mathbf{r}-\omega_1 t)]+\hat{\mathbf{e}}_2 A_2(t)\exp[i(\mathbf{k}_2\cdot\mathbf{r}-\omega_2 t)]+\hat{\mathbf{e}}_3 A_3(t)\exp[i(\mathbf{k}_3\cdot\mathbf{r}-\omega_1 t)]+\text{c.c.}\} , \tag{6}$$

where fields A_1 and A_3 have the same frequency ω_1, but will in general have different propagation directions. For simplicity, we will assume that $\hat{\mathbf{e}}_1=\hat{\mathbf{e}}_3$, $\mathbf{k}_1=\mathbf{k}_3$, and that $A_i=A_i^*$. Furthermore, we will solve the density-matrix equations for $\mathbf{r}=0$ only. We can redefine the amplitude A_1 as the sum of amplitudes A_1 and A_3. The electric field is thus given by

$$\mathbf{E}(t)=\tfrac{1}{2}[\hat{\mathbf{e}}_1 A_1(t)e^{-i\omega_1 t}+\hat{\mathbf{e}}_2 A_2(t)e^{-i\omega_2 t}+\text{c.c.}] . \tag{7}$$

Equations (3) and (4) must be manipulated for computer solution. For clarity in this paper, the indices j, k, and m will be assigned hereafter to states in the ground electronic level, and the indices p, q, and s will be assigned to states in the excited electronic level. We will separate the solution of Eqs. (3) and (4) into the following three cases: (1) upper level p and lower level j, (2) lower levels j and k, and (3) upper levels p and q.

1. Case 1: Coupling between upper level p and lower level j

When p is an upper level and j is a lower level, the off-diagonal matrix elements ρ_{pj} will be driven at frequencies close to ω_1. Consequently, we can define the slowly varying quantity σ_{pj},

$$\rho_{pj}=\sigma_{pj}e^{-i\omega_1 t} . \tag{8}$$

Substituting Eq. (8) into Eq. (4) and multiplying both sides of the equation by $e^{+i\omega_1 t}$ gives

$$\dot{\sigma}_{pj}=i(\omega_1-\omega_{pj})\sigma_{pj}-\gamma_{pj}\sigma_{pj}-\frac{i}{\hbar}V_{pj}e^{+i\omega_1 t}(\rho_{jj}-\rho_{pp})-\frac{i}{\hbar}\sum_m V_{pm}e^{+i\omega_1 t}\rho_{mj}+\frac{i}{\hbar}\sum_s \rho_{ps}V_{sj}e^{+i\omega_1 t} . \tag{9}$$

The notations m and s under the summation signs denote summation over all states in the ground and excited electronic levels, respectively. It is helpful to define the radiative interaction terms $\Omega_{pm}=V_{pm}e^{+i\omega_1 t}/\hbar$, $\Omega_{pj}=V_{pj}e^{+i\omega_1 t}$, and $\Omega_{sj}=V_{sj}e^{+i\omega_1 t}/\hbar$. Rewriting these expressions in terms of real and imaginary parts and neglecting terms that oscillate at optical frequencies in accordance with the rotating-wave approximation gives

$$\Omega_{pm}^r=-\frac{1}{2\hbar}[d_{pm}^{1r}A_1+d_{pm}^{2r}A_2\cos(\Delta t)-d_{pm}^{2i}A_2\sin(\Delta t)] , \tag{10}$$

$$\Omega_{pm}^i=-\frac{1}{2\hbar}[d_{pm}^{1i}A_1+d_{pm}^{2i}A_2\cos(\Delta t)+d_{pm}^{2r}A_2\sin(\Delta t)] , \tag{11}$$

and similar expressions for Ω_{pj} and Ω_{sj}. The radiative interaction terms Ω_{pm}, Ω_{pj}, and Ω_{sj} have units corresponding to Rabi frequencies, but they account for the interaction of both laser fields with the resonance pm, pj, or sj and are modulated at the beat frequency Δ between the two laser fields. In Eqs. (10) and (11), the dipole matrix element $d_{pm}^{1r}=\mathbf{d}_{pm}^r\cdot\hat{\mathbf{e}}_1$, $d_{pm}^{2r}=\mathbf{d}_{pm}^r\cdot\hat{\mathbf{e}}_2$, etc. The superscripts r and i refer to real and imaginary components, respectively. The quantity $\Delta=\omega_1-\omega_2$.

Solving Eq. (9) for the real and imaginary parts of the off-diagonal matrix elements gives the following set of equations:

$$\dot{\sigma}_{pj}^r=-(\omega_1-\omega_{pj})\sigma_{pj}^i-\gamma_{pj}\sigma_{pj}^r+\Omega_{pj}^i(\rho_{jj}-\rho_{pp})+\sum_m(\Omega_{pm}^r\rho_{mj}^i+\Omega_{pm}^i\rho_{mj}^r)-\sum_s(\rho_{ps}^r\Omega_{sj}^i+\rho_{ps}^i\Omega_{sj}^r) , \tag{12}$$

$$\dot{\sigma}^{i}_{pj}=(\omega_1-\omega_{pj})\sigma^{r}_{pj}-\gamma_{pj}\sigma^{i}_{pj}-\Omega^{r}_{pj}(\rho_{jj}-\rho_{pp})+\sum_{m}(-\Omega^{r}_{pm}\rho^{r}_{mj}+\Omega^{i}_{pm}\rho^{i}_{mj})+\sum_{s}(\rho^{r}_{ps}\Omega^{r}_{sj}-\rho^{i}_{ps}\Omega^{i}_{sj}) . \quad (13)$$

2. Case 2: Coupling between lower levels k and j

(a) $k\neq j$. We assume that the single-photon, electric dipole matrix element between lower levels can be neglected. Consequently, in Eq. (4) we will sum only over upper levels s,

$$\dot{\rho}_{kj}=-\rho_{kj}(i\omega_{kj}+\gamma_{kj})-\frac{i}{\hbar}\sum_{s}(V_{ks}\rho_{sj}-\rho_{ks}V_{sj}) . \quad (14)$$

The off-diagonal element ρ_{kj} oscillates with a frequency close to ω_{kj}, much less than the typical optical frequency ω_1. On the other hand, the off-diagonal elements ρ_{sj} and ρ_{ks} oscillate with frequencies close to ω_1, as discussed in Sec. II A 1. In terms of the slowly varying quantities σ_{sj} and σ_{ks}, Eq. (14) becomes

$$\dot{\rho}_{kj}=-\rho_{kj}(i\omega_{kj}+\gamma_{kj})-\frac{i}{\hbar}\sum_{s}(V_{ks}\sigma_{sj}e^{-i\omega_1 t}-\sigma_{ks}e^{+i\omega_1 t}V_{sj}) . \quad (15)$$

As in Sec. II A 1, the radiative interaction terms $\Omega_{ks}=V_{ks}e^{-i\omega_1 t}/\hbar$ and $\Omega_{sj}=V_{sj}e^{+i\omega_1 t}/\hbar$ are defined as follows:

$$\Omega^{r}_{ks}=-\frac{1}{2\hbar}[d^{1r}_{ks}A_1+d^{2r}_{ks}A_2\cos(\Delta t)+d^{2i}_{ks}A_2\sin(\Delta t)] , \quad (16)$$

$$\Omega^{i}_{ks}=-\frac{1}{2\hbar}[d^{1i}_{ks}A_1+d^{2i}_{ks}A_2\cos(\Delta t)-d^{2r}_{ks}A_2\sin(\Delta t)] , \quad (17)$$

$$\Omega^{r}_{sj}=-\frac{1}{2\hbar}[d^{1r}_{sj}A_1+d^{2r}_{sj}A_2\cos(\Delta t)-d^{2i}_{sj}A_2\sin(\Delta t)] , \quad (18)$$

$$\Omega^{i}_{sj}=-\frac{1}{2\hbar}[d^{1i}_{sj}A_1+d^{2i}_{sj}A_2\cos(\Delta t)+d^{2r}_{sj}A_2\sin(\Delta t)] . \quad (19)$$

Equations (16)–(19) are very similar to Eqs. (10) and (11) but they are not identical. Solving for the real and imaginary parts of $\dot{\rho}_{kj}$ in terms of Ω_{ks} and Ω_{sj} gives

$$\dot{\rho}^{r}_{kj}=\omega_{kj}\rho^{i}_{kj}-\gamma_{kj}\rho^{r}_{kj}+\sum_{s}(\Omega^{r}_{ks}\sigma^{i}_{sj}+\Omega^{i}_{ks}\sigma^{r}_{sj}-\sigma^{r}_{ks}\Omega^{i}_{sj}-\sigma^{i}_{ks}\Omega^{r}_{sj}) , \quad (20)$$

$$\dot{\rho}^{i}_{kj}=-\omega_{kj}\rho^{r}_{kj}-\gamma_{kj}\rho^{i}_{kj}+\sum_{s}(-\Omega^{r}_{ks}\sigma^{r}_{sj}+\Omega^{i}_{ks}\sigma^{i}_{sj}+\sigma^{r}_{ks}\Omega^{r}_{sj}-\sigma^{i}_{ks}\Omega^{i}_{sj}) . \quad (21)$$

(b) $k=j$. Manipulating Eq. (3) for the diagonal matrix element in a similar fashion and using the same definitions for Ω_{ks} and Ω_{sk} [Eqs. (16)–(19)], we obtain

$$\dot{\rho}_{kk}=-\Gamma_k\rho_{kk}+\sum_{s}\Gamma_{sk}\rho_{ss}+\sum_{m\neq k}\Gamma_{mk}\rho_{mm}+\sum_{s}(\Omega^{r}_{ks}\sigma^{i}_{sk}+\Omega^{i}_{ks}\sigma^{r}_{sk}-\sigma^{r}_{ks}\Omega^{i}_{sk}-\sigma^{i}_{ks}\Omega^{r}_{sk}) , \quad (22)$$

Equation (22) describes the time dependence of the population for level k.

3. Case 3: Coupling between upper levels p and q

(a) $p\neq q$. The derivation for case 3 is very similar to that for case 2. We again assume that the electric dipole matrix elements between upper levels can be neglected. In Eq. (4) we will sum only over lower levels m,

$$\dot{\rho}_{pq}=-\rho_{pq}(i\omega_{pq}+\gamma_{pq})-\frac{i}{\hbar}\sum_{m}(V_{pm}\rho_{mq}-\rho_{pm}V_{mq}) . \quad (23)$$

In terms of the slowly varying quantities σ_{mq} and σ_{pm}, Eq. (23) becomes

$$\dot{\rho}_{pq}=-\rho_{pq}(i\omega_{pq}+\gamma_{pq})-\frac{i}{\hbar}\sum_{m}(V_{pm}\sigma_{mq}e^{+i\omega_1 t}-\sigma_{pm}e^{-i\omega_1 t}V_{mq}) . \quad (24)$$

We define the quantities $\Omega_{pm}=V_{pm}e^{+i\omega_1 t}/\hbar$ and $\Omega_{mq}=V_{mq}e^{-i\omega_1 t}/\hbar$ as in Eqs. (16)–(19). Solving for the real and imaginary parts of $\dot{\rho}_{pq}$ in terms of Ω_{pm} and Ω_{mq} gives

$$\dot{\rho}^{r}_{pq}=\omega_{pq}\rho^{i}_{pq}-\gamma_{pq}\rho^{r}_{pq}+\sum_{m}(\Omega^{r}_{pm}\sigma^{i}_{mq}+\Omega^{i}_{pm}\sigma^{r}_{mq}-\sigma^{r}_{pm}\Omega^{i}_{mq}-\sigma^{i}_{pm}\Omega^{r}_{mq}) , \quad (25)$$

$$\dot{\rho}^{i}_{pq}=-\omega_{pq}\rho^{r}_{pq}-\gamma_{pq}\rho^{i}_{pq}+\sum_{m}(-\Omega^{r}_{pm}\sigma^{r}_{mq}+\Omega^{i}_{pm}\sigma^{i}_{mq}+\sigma^{r}_{pm}\Omega^{r}_{mq}-\sigma^{i}_{pm}\Omega^{i}_{mq}) . \quad (26)$$

(*b*) $p=q$. As for case 2, we can solve Eq. (3) for the diagonal matrix element

$$\dot{\rho}_{pp}=-\Gamma_p\rho_{pp}+\sum_s\Gamma_{sp}\rho_{ss}+\sum_m(\Omega^r_{pm}\sigma^i_{mp}+\Omega^i_{pm}\sigma^r_{mp}-\sigma^r_{pm}\Omega^i_{mp}-\sigma^i_{pm}\Omega^r_{mp}) . \tag{27}$$

B. Solution of the density-matrix equations and calculation of the medium polarization

Equations (12), (13), (20)–(22), and (25)–(27) are integrated numerically to give the time-dependent diagonal and off-diagonal density-matrix elements for a multilevel system interacting with two laser beams. The medium polarization serves as the source term in Maxwell's equations for the higher-order wave-mixing signals. In terms of the density-matrix elements, the medium polarization $\mathbf{P}(t)$ is given by [33]

$$\mathbf{P}(t)=\mathrm{Tr}[\rho(t)\mathbf{d}]=\sum_s\sum_m\rho_{sm}(t)\mathbf{d}_{ms} . \tag{28}$$

Nonzero density-matrix elements exist only between upper levels s and lower levels m. In terms of slowly varying components, Eq. (28) becomes

$$\mathbf{P}(t)=\sum_m\sum_s\sigma_{ms}e^{+i\omega_1 t}\mathbf{d}_{sm}+\sum_s\sum_m\sigma_{sm}e^{-i\omega_1 t}\mathbf{d}_{ms} . \tag{29}$$

The polarization $\mathbf{P}(t)$ has polarization components aligned with the polarizations $\hat{\mathbf{e}}_1$ and $\hat{\mathbf{e}}_2$ of fields 1 and 2:

$$P_1(t)=\sum_m\sum_s\sigma_{ms}e^{+i\omega_1 t}d^1_{sm}+\sum_s\sum_m\sigma_{sm}e^{-i\omega_1 t}d^1_{ms}=P_1^+(t)e^{+i\omega_1 t}+P_1^-(t)e^{-i\omega_1 t} , \tag{30}$$

$$P_2(t)=\sum_m\sum_s\sigma_{ms}e^{+i\omega_1 t}d^2_{sm}+\sum_s\sum_m\sigma_{sm}e^{-i\omega_1 t}d^2_{ms}=P_2^+(t)e^{+i\omega_1 t}+P_2^-(t)e^{-i\omega_1 t} . \tag{31}$$

Multiwave-mixing intensities are calculated by Fourier analysis of the polarizations $P_1(t)$ and $P_2(t)$. For example, the four-wave-mixing signal with polarization $\hat{\mathbf{e}}_2$ is given by the power spectrum of $P_2(t)$ with respect to $2\omega_1-\omega_2$,

$$S_4(2\omega_1-\omega_2)=\left|\int P_2(t)e^{-i(2\omega_1-\omega_2)t}dt\right|^2=\left|\int P_2^+(t)e^{-i(\omega_1-\omega_2)t}dt\right|^2 ; \tag{32}$$

the six-wave-mixing signal is given by

$$S_6(3\omega_1-2\omega_2)=\left|\int P_2(t)e^{-i(3\omega_1-2\omega_2)t}dt\right|^2=\left|\int P_2^+(t)e^{-i(2\omega_1-2\omega_2)t}dt\right|^2 ; \tag{33}$$

and the eight-wave-mixing signal is given by

$$S_8(4\omega_1-3\omega_2)=\left|\int P_2(t)e^{-i(4\omega_1-3\omega_2)t}dt\right|^2=\left|\int P_2^+(t)e^{-i(3\omega_1-3\omega_2)t}dt\right|^2 . \tag{34}$$

In Eqs. (32)–(34), terms that oscillate at optical frequencies are neglected in the numerical integration. Fourier analysis of the polarization in these calculations serves the same purpose as phase matching in the experiments by selecting only certain frequency components that arise from the wave-mixing process. Experimentally and computationally, higher-order wave-mixing components may contribute to a wave-mixing signal of a certain order. For example, the calculated eight-wave-mixing (8WM) signal may also contain contributions due to wave-mixing processes of order 10, 12, etc. These processes are obtained by adding and subtracting one or more of either input frequency (or **k** vector) in the phase-matching equations. All of these wave-mixing processes are also allowed in an 8WM phase-matching geometry [10,20]. Of course, this interpretation will not hold when perturbation theory breaks down.

It should also be noted that the Fourier analysis of the calculated polarization breaks down at zero frequency difference ($\omega_1=\omega_2$). At zero frequency difference it is no longer possible to distinguish the various wave-mixing orders. Experimentally, geometric phase matching discriminates among wave-mixing orders even for degenerate beams.

III. MULTIWAVE-MIXING CALCULATIONS FOR A THREE-LEVEL SYSTEM

A. Multiwave-mixing interactions in the three-level system

In this section the numerical analysis of multiwave mixing described in Sec. II is applied to a three-level system consisting of two ground levels of nearly equal energy and one excited electronic level. Some of the essential physics of the multiwave-mixing interaction will be illustrated by first considering this relatively simple three-level system irradiated by laser beams with parallel polarization. Later, the more complex case of a 16-level system irradiated by two laser beams with perpendicular polarizations will be considered.

The three-level system is schematically illustrated in Fig. 4. We assume that both ground levels are radiatively

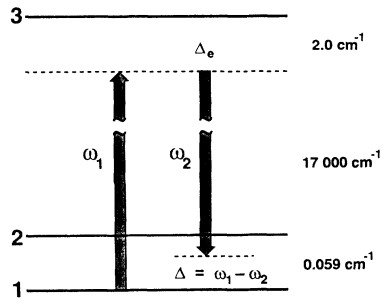

FIG. 4. Energy-level diagram for the three-level system.

TABLE I. Values of the collisional rates used in the three-level model calculations.

Coherence dephasing collision rates	
Ground-state coherence	$\gamma_{12}=\gamma_{21}=2.0\times10^{8}$ sec^{-1}
Electronic resonance	$\gamma_{13}=\gamma_{31}=\gamma_{12}=\gamma_{23}=5.0\times10^{9}$ sec^{-1}
Population transfer collision rates	
Ground states	$\Gamma_{12}=\Gamma_{21}=1.0\times10^{6}$ sec^{-1}
Electronic transfer	$\Gamma_{32}=\Gamma_{31}=5.0\times10^{8}$ sec^{-1}
	$\Gamma_{23}=\Gamma_{13}=0$

coupled to the excited electronic level by both of the nearly degenerate laser beams. The collisional parameters for the three-level system are summarized in Table I. The dipole-moment matrix elements $d^1_{13}=d^1_{23}=d^2_{13}=d^2_{23}$ are assumed to be real.

The laser beams are assumed to be linearly polarized in the same direction [$\hat{e}_1=\hat{e}_2$, $P_1(t)=P_2(t)=P(t)$]. The laser pulse shape is modeled as Gaussian with a full width at half maximum (FWHM) of 15 ns for the electric-field amplitude, or 10 ns for the laser intensity. This FWHM is less than the experimentally measured FWHM of 20 ns for the laser intensity [10]. The frequency bandwidth of the experimental laser pulse was slightly less than 0.002 cm^{-1}, or about twice the Fourier-transform limit. The frequency bandwidth of the 10-ns laser pulse used in the calculations is therefore comparable to the experimental value. Some calculations were performed with 20-ns pulses that were chirped [34] so as to give the same bandwidth as the experimental pulses, and with unchirped 20-ns pulses. For the same peak laser intensity, calculated spectra were nearly identical for all of these cases. To reduce computational time, most of the calculations were performed with the 10-ns pulses.

The coherent-excitation dynamics of various three-level atomic systems has been reviewed by Shore [31]. In studies [31,35–37] of the Λ system, it is assumed generally that each laser field interacts with only one of the transitions that couple the ground and excited states (1-3 and 2-3) either because of the large splitting between ground states or because of the polarization properties of the laser radiation. The phenomenon of population trapping in the ground states of such a system has been widely studied. In the calculations presented in this section, both laser fields interact with both of the transtions 1-3 and 2-3. As will be seen in Sec. III C, at high intensity population is pumped from one of the ground states to the other ground state by the coherent excitation. However, the main focus of our investigation is the multiwave-mixing interaction in the three-level system.

B. Intensity dependence of the multiwave-mixing spectra

Four-wave-mixing spectra in the three-level system are shown in Fig. 5. As the laser intensity increases (the Rabi frequency

$$\Omega_R=\Omega_{R1}=\Omega_{R2}=dA_1/2\hbar c=dA_2/2\hbar c$$

in units of cm^{-1}), the four-wave mixing component at $\omega_{\rm hfs}=0.059$ cm^{-1} broadens noticeably and an additional spectral component appears at $\omega_{\rm hfs}/2$. Six- and eight-wave-mixing spectra are shown in Figs. 6 and 7. The six-wave-mixing (6WM) spectra are dominated by the spectral feature at $\omega_{\rm hfs}/2$, which broadens noticeably with increasing laser intensity. The 8WM spectra show much more interesting behavior. At the lowest laser intensity shown, only a single spectral component at $\omega_{\rm hfs}/3$ is evident in the 8WM spectrum. As the laser intensity increases, however, additional components at $\omega_{\rm hfs}/2$ and $\omega_{\rm hfs}/4$ also become noticeable. In addition, the peaks of these lines have shifted to higher frequency difference. As will be seen in Sec. III C, the drastic change in the character of the spectrum with laser intensity corre-

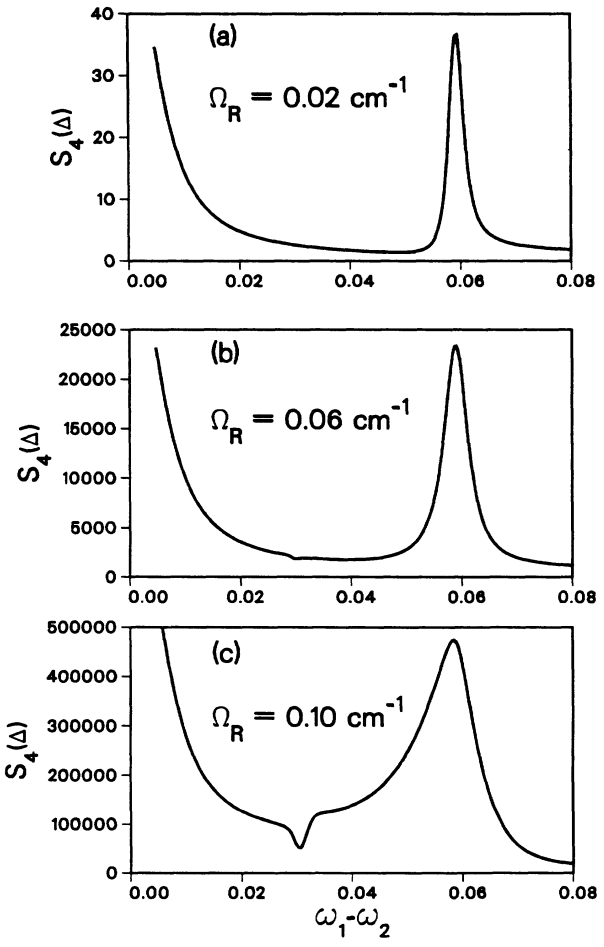

FIG. 5. Four-wave-mixing spectra for the three-level system for Rabi frequencies of (a) 0.02, (b) 0.06, and (c) 0.10 cm^{-1}.

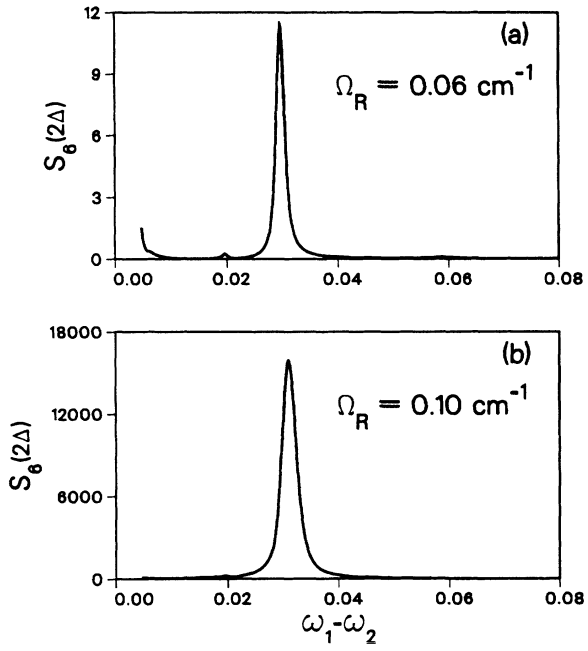

FIG. 6. Six-wave-mixing spectra for the three-level system for Rabi frequencies of (a) 0.06 and (b) 0.10 cm^{-1}.

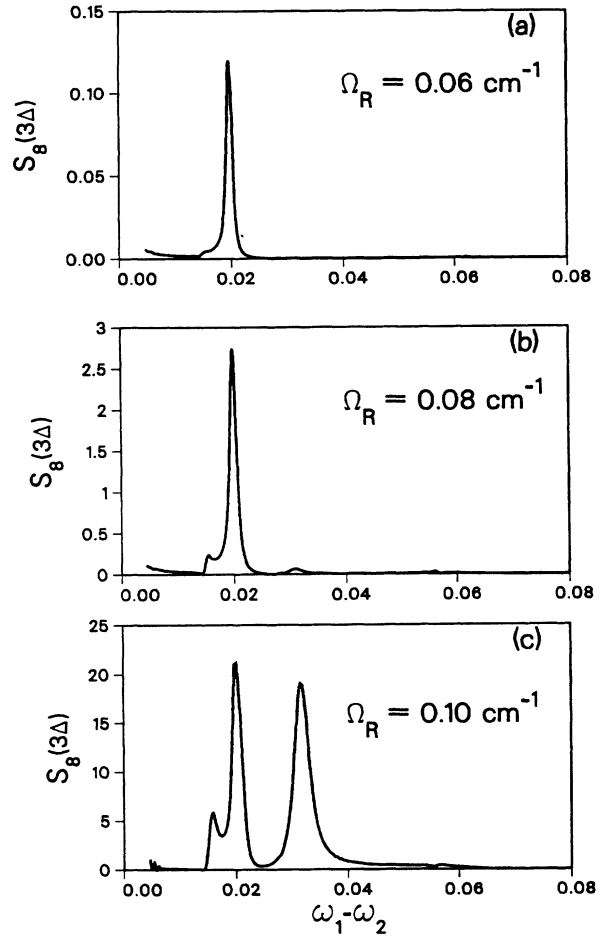

FIG. 7. Eight-wave-mixing spectra for the three-level system for Rabi frequencies of (a) 0.06, (b) 0.08, and (c) 0.10 cm^{-1}.

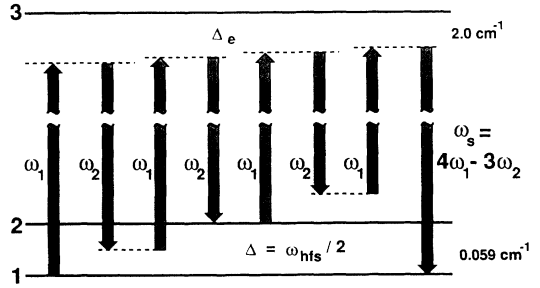

FIG. 8. Energy-level diagram for eight-wave mixing in the three-level system for a laser detuning $\omega_1-\omega_2=\omega_{hfs}/2$.

sponds to the onset of significant population transfer in the three-level system.

Consider the energy-level diagrams of the 8WM processes shown in Figs. 8 and 9. From the viewpoint of perturbation theory, the 8WM signal arises from the scattering of a photon at ω_1 by a ground-level coherence oscillating at a frequency $3(\omega_1-\omega_2)$. This ground-level coherence is induced by a six-photon process, probed by a single photon. For the spectral component at $\omega_{hfs}/3$, the six-photon process is resonant. The component at $\omega_{hfs}/2$ is due to a four-photon resonant process probed by three photons. Similarly, the component at ω_{hfs}, just barely visible in Fig. 7, is due to a two-photon resonant process probed by a five-photon process.

The relative intensities of the components at $\omega_{hfs}/2$ and $\omega_{hfs}/3$ are obviously quite sensitive to laser intensity. The resonance at $\omega_{hfs}/2$ is barely visible at low laser intensity, but becomes comparable in intensity to the resonance at $\omega_{hfs}/3$ at high laser intensity. One possible explanation for this is that an 8WM selection rule prohibits the $\omega_{hfs}/2$ resonance, but it is allowed for higher-order processes. Selection rules could prohibit this resonance in 8WM, even though all single-photon dipole matrix elements are set equal to each other and are real, because of cancellations in the various possible two-photon processes that give rise to the four-photon resonance. Because the resonance at $\omega_{hfs}/2$ is exactly midway between states 1 and 2, two-photon processes beginning at state 1 may interfere destructively with processes beginning at state 2.

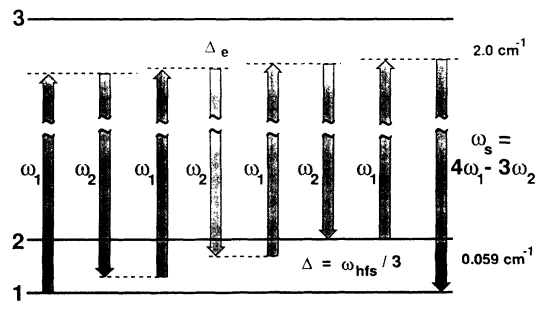

FIG. 9. Energy-level diagram for eight-wave mixing in the three-level system for a laser detuning $\omega_1-\omega_2=\omega_{hfs}/3$.

The detuning for these two-photon processes will have equal magnitude but opposite sign, leading to cancellations in the 8WM process. In ten-wave mixing (10WM), such cancellations may not occur and the resonance at $\omega_{hfs}/2$ could become quite strong compared to the resonance at $\omega_{hfs}/3$ as laser intensity increased.

Again from the viewpoint of perturbation theory, another possible explanation for this behavior is population pumping. At low laser intensity, terms proportional to $(\rho_{11}-\rho_{22})$ are negligible compared to the collision-induced terms because the populations of the hyperfine levels are equal. As will be shown in Sec. III C at higher laser intensity the populations are no longer equal due to population pumping, and terms proportional to $(\rho_{11}-\rho_{22})$ may become significant.

The spectra shown in Figs. 5–7 were calculated by integrating Eqs. (12), (13), (20)–(22), and (27) for successive values of ω_2 (ω_1 was fixed) to obtain the time-dependent on- and off-diagonal matrix elements. A fifth-order Adams-Bashforth predictor-corrector method, subroutine DEABM in the Sandia FORTRAN SLATEC library, was used for the numerical integration. The time step of the numerical integration was decreased until the solution converged; for an electronic detuning $\Delta_e=2$ cm^{-1}, a time step of 1 psec was used. This large detuning from electronic resonance induces the fastest fluctuations in the numerical solution, and the required time step is inversely proportional to the detuning in this study. Integration for 80 nsec over a laser pulse to obtain a single intensity point in the spectrum required approximately 4 min of CPU time on a DEC station 3100 (MIPS R2000 CPU and R2010 FPU chips).

C. Temporal evolution of the density-matrix elements

In this section the temporal response of the three-level system to the laser pulse at ω_1 and ω_2 is discussed in detail. The temporal response of the system will be discussed in terms of the time dependence of the level populations $[\rho_{11}(t), \rho_{22}(t), \rho_{33}(t)]$, the ground-level coherence $[\rho_{12}(t)]$, and the induced polarization $[P(t)]$. Specifically, the case where $\omega_1-\omega_2=0.03$ cm^{-1} and $\Delta_e=2.0$ cm^{-1} will be considered, and the physics of the 6WM resonance will be explored. The temporal response of the system will be considered at varying laser intensity to illustrate the strong coupling between population transfer and the induced polarization that presumably influences strongly the strength of the observed subharmonic resonances.

The time dependence of the level populations at three different laser intensities is shown in Fig. 10. The calculations proceed for 80 nsec, with the laser pulses peaking at 40 nsec. At low laser intensity [Fig. 10(a)], the level populations exhibit a beat frequency corresponding to the difference of the laser frequencies, $\omega_1-\omega_2=0.03$ cm^{-1}.

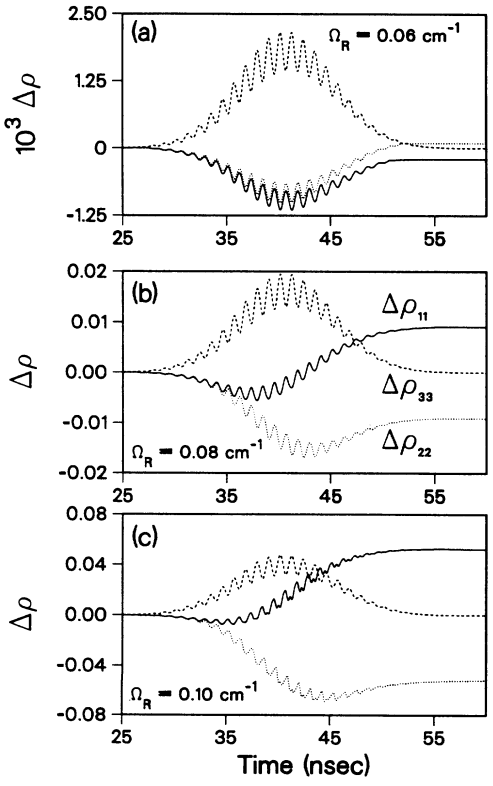

FIG. 10. Time dependence of the level populations for the three-level system for Rabi frequencies of (a) 0.06, (b) 0.08, and (c) 0.10 cm^{-1}. The laser detuning $\omega_1-\omega_2=\omega_{hfs}/2$.

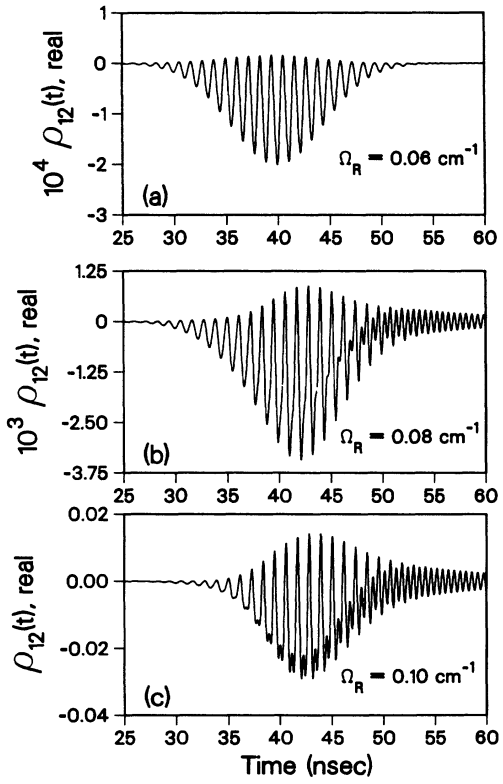

FIG. 11. Time dependence of the real part of the off-diagonal matrix element $\rho_{21}(t)$ for the three-level system for Rabi frequencies of (a) 0.06, (b) 0.08, and (c) 0.10 cm^{-1}. The laser detuning $\omega_1-\omega_2=\omega_{hfs}/2$.

The time dependence of the ground-level coherence $\rho_{12}(t)$ (imaginary part) is shown in Fig. 11. Again, at low laser intensity $\rho_{12}(t)$ exhibits a beat frequency corresponding to the difference of laser frequencies.

As the laser intensity increases, however, the change in level populations becomes significant and the coupling between the level populations and the induced polarization becomes apparent. In Figs. 10(b) and 11(b), it is obvious that the ground-level populations $\rho_{11}(t)$ and $\rho_{22}(t)$ and the ground-level coherence $\rho_{12}(t)$ are modulated at a frequency (or frequencies) higher than the laser difference frequency. As population transfer becomes significant (fractional population change of approximately 5%), the equations describing the time development of the on- and off-diagonal components of the density matrix become strongly coupled. This coupling will strongly affect the strength of the subharmonic resonance.

While the modulation of the ground-level coherence at higher frequencies is obvious in Figs. 11(b) and 11(c), the appearance of higher-order frequencies in the polarization $P(t)$ is not at all obvious. The real and imaginary parts of $P^+(t)$ are plotted in Fig. 12 for low and high laser intensity. The shapes of the wave forms in Fig. 12 are very similar and it is hard to discern any contribution from higher-order frequencies. The contribution of the modulation frequency that gives rise to the six-wave-mixing signal can be seen more clearly by plotting the function $G(t)$, where

$$G(t)=\int_0^t P^+(\tau)e^{-i(2\omega_1-2\omega_2)\tau}d\tau\ . \tag{35}$$

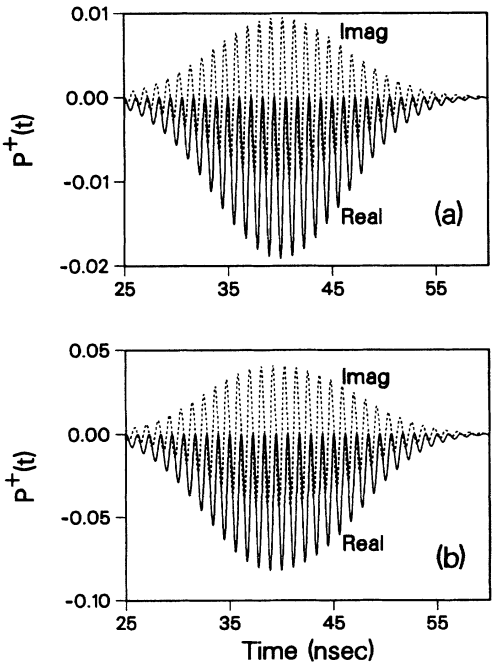

FIG. 12. Time dependence of the real and imaginary parts of the induced polarization $P^+(t)=P(t)e^{+i\omega_1 t}$ for the three-level system for Rabi frequencies of (a) 0.06 and (b) 0.10 cm^{-1}. The laser detuning $\omega_1-\omega_2=\omega_{hfs}/2$.

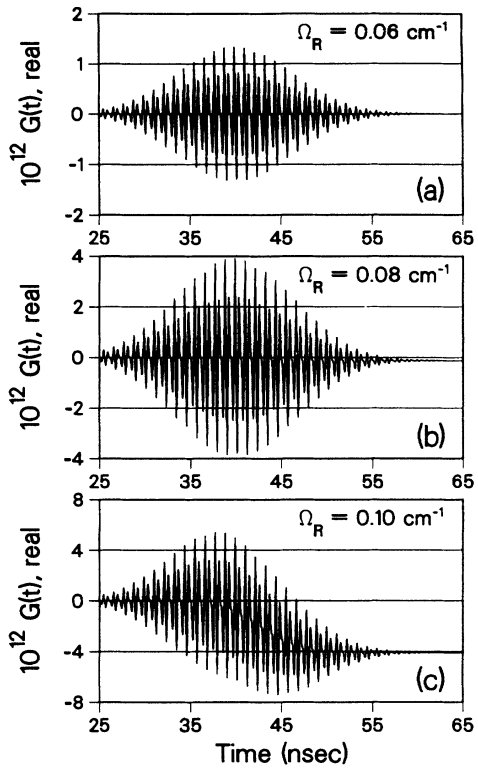

FIG. 13. Time dependence of the real part of the integral function $G(t)$ for the three-level system for Rabi frequencies of (a) 0.06, (b) 0.08, and (c) 0.10 cm^{-1}. The laser detuning $\omega_1-\omega_2=\omega_{hfs}/2$.

For time t long enough to include the entire laser pulse, the six-wave-mixing signal is given by $|G(t)|^2$. The function $G(t)$ is plotted for three different values of the laser intensity in Fig. 13. For low intensity, both the real and imaginary parts of $G(t)$ oscillate around zero and reach a limiting value very close to zero compared to their peak oscillation amplitudes. For higher intensity, the oscillation of the function becomes less symmetric as the laser pulse proceeds and the limiting value of the function is significant compared to the oscillation amplitude, i.e., the six-wave-mixing signal is becoming stronger. It is obvious from the highest intensity spectrum plotted, Fig. 13(c), that substantial deviation from symmetric oscillation about zero begins to occur at approximately the same point in the laser pulse that significant population transfer occurs. Note that even for Fig. 13(c) the higher-order contribution is extremely small relative to the amplitude of the medium polarization $P^+(t)$; it is not surprising that no higher frequencies are evident in Fig. 12.

IV. MULTIWAVE-MIXING CALCULATIONS FOR THE $3\,^2S_{1/2}$–$3\,^2P_{1/2}$ SYSTEM OF THE SODIUM ATOM

The 4WM and 6WM spectra calculated for a three-level system, shown in Figs. 5 and 6, are qualitatively similar to the spectra observed experimentally. However,

for the case of 8WM, the calculated relative intensities of the spectral features differ markedly even for the low laser intensity. Although the three-level calculations are helpful for understanding the physics of higher-order wave-mixing processes, the actual electric dipole interaction matrix elements, the hyperfine splitting in the excited electronic state, the Zeeman-sublevel structure in both the ground and the excited states, and the polarization properties of the laser beams must be included in the calculation to obtain better agreement with experiment. In this section the results of including all of these effects in a 16-level model of multiwave-mixing interactions with the sodium $3\,^2S_{1/2}$–$3\,^2P_{1/2}$ electronic resonance are presented. The agreement between theory and experiment is markedly improved over that of the three-level model.

A. Radiative and collisional interactions in the 16-level system

The relative dipole matrix elements for the electronic resonance were derived from the angular part of the one-electron wave functions that include both electron and nuclear spin. Spin orbit ($\mathbf{L}\cdot\mathbf{S}$) and hyperfine ($\mathbf{J}\cdot\mathbf{I}$) coupling interactions were then sequentially applied to these normalized wave functions [38]. Matrix elements of the $\hat{\mathbf{e}}_z$ and $\hat{\mathbf{e}}_x$ components of the electric dipole moment between these states are listed in Tables II and III. The polarization vector $\hat{\mathbf{e}}_1$ is assumed to be aligned with the magnetic orientation z axis of the sodium atoms. The polarization vector $\hat{\mathbf{e}}_2$ is aligned with the x axis. For this polarization orientation, both d^1_{ms} and d^2_{ms} are real quantities, where m and s are any two lower and upper states, respectively. The dipole matrix elements are normalized such that, for a single state (F,m_F), the sum of the squares of the dipole matrix elements for all transitions is equal to $\frac{1}{3}$ for a particular polarization, or unity for all three polarizations. The radial part of the nonzero matrix elements, determined using a radiative lifetime of 16.3 nsec, is 6.33 D. Based on our definition of Rabi frequency $\Omega_R = dA/2\hbar c$, the Rabi frequency for a given transition in the $3\,^2S_{1/2}$–$3\,^2P_{1/2}$ system is equal to 0.168 cm^{-1} times the value given in Table II or III for a laser intensity of 10 kW/cm^2.

The collisional dephasing and population transfer rates used for the higher-order wave-mixing calculations in the $3\,^2S_{1/2}$–$3\,^2P_{1/2}$ system are listed in Table IV. Because the experiments of Trebino and Rahn [10] were performed in an atmospheric pressure, hydrogen-air flat flame, the collisional transfer rates are difficult to calculate accurately due to a lack of information about high-temperature collisional cross sections and to uncertainty in the actual flame temperature due to heat losses to the burner. However, after performing numerous calculations with different collisional rates, it appears that the calculated spectra are sensitive mostly to the dephasing rate γ_{km} for the ground-level coherence. The dephasing rate for the electronic resonance γ_{sm} affects the strength of the spectra but has relatively little effect on the calculated spectral line shapes and relative intensities of the spectral features.

Fourkas *et al.* [39] recently determined the electronic quenching rate and ground-state dephasing rate from measured grating decay times for sodium seeded into a methane-air flame. They reported a population grating decay time of 400 psec, corresponding to an electronic quenching rate $\Gamma_{sm} = 1.2\times10^9$ sec^{-1}. A ground-state hyperfine dephasing rate $\gamma_{km} = 2\times10^8$ sec^{-1} was determined from the decay of the polarization grating. These values are close to those listed in Table IV. In a flame very similar to that used by Trebino and Rahn [10], Goldsmith [40] measured the homogeneous width [half width at half maximum (HWHM)] of the $3\,^2S_{1/2}$–$3\,^2P_{3/2}$ transition to be approximately 2.7 GHz, corresponding to a dephasing collision rate of $\gamma_{sm} = 1.7\times10^{10}$ sec^{-1}. This value must be regarded as an upper limit because of the ground-state splitting of 1.8 GHz (0.059 cm^{-1}). The value of $\gamma_{sm} = 5.0\times10^9$ sec^{-1} listed in Table IV seems quite reasonable compared to the value measured by Goldsmith for a similar transition.

B. Comparison of calculated and experimental multiwave-mixing spectra

In this section calculated multiwave-mixing spectra are compared with the experimental results of Trebino and

TABLE II. Relative values of the z component of the electric dipole matrix elements for the sodium $3\,^2P_{1/2}$–$3\,^2S_{1/2}$ electronic resonance. The z-component values are all real quantities.

$\mathbf{d}\cdot\hat{\mathbf{e}}_z$		$F=2$	$F=2$	$F=2$	$F=2$	$F=2$	$F=1$	$F=1$	$F=1$
$3\,^2S_{1/2}$	$3\,^2P_{1/2}$	$m_F=2$	$m_F=1$	$m_F=0$	$m_F=-1$	$m_F=-2$	$m_F=1$	$m_F=0$	$m_F=-1$
$F=2$	$m_F=2$	$-1/\sqrt{3}$	0	0	0	0	0	0	0
$F=2$	$m_F=1$	0	$-1/2\sqrt{3}$	0	0	0	1/2	0	0
$F=2$	$m_F=0$	0	0	0	0	0	0	$1/\sqrt{3}$	0
$F=2$	$m_F=-1$	0	0	0	$1/2\sqrt{3}$	0	0	0	1/2
$F=2$	$m_F=-2$	0	0	0	0	$1/\sqrt{3}$	0	0	0
$F=1$	$m_F=1$	0	1/2	0	0	0	$1/2\sqrt{3}$	0	0
$F=1$	$m_F=0$	0	0	$1/\sqrt{3}$	0	0	0	0	0
$F=1$	$m_F=-1$	0	0	0	1/2	0	0	0	$-1/2\sqrt{3}$

TABLE III. Relative values of the x component of the electric dipole matrix elements for the sodium $3\,^2P_{1/2}$–$3\,^2S_{1/2}$ electronic resonance. The x-component values are all real quantities.

$\mathbf{d}\cdot\hat{\mathbf{e}}_x$		$F=2$	$F=2$	$F=2$	$F=2$	$F=2$	$F=1$	$F=1$	$F=1$
$3\,^2S_{1/2}$	$3\,^2P_{1/2}$	$m_F=2$	$m_F=1$	$m_F=0$	$m_F=-1$	$m_F=-2$	$m_F=1$	$m_F=0$	$m_F=-1$
$F=2$	$m_F=2$	0	$-1/2\sqrt{3}$	0	0	0	$1/2$	0	0
$F=2$	$m_F=1$	$-1/2\sqrt{3}$	0	$-1/2\sqrt{2}$	0	0	0	$-1/2\sqrt{2}$	0
$F=2$	$m_F=0$	0	$-1/2\sqrt{2}$	0	$-1/2\sqrt{2}$	0	$1/2\sqrt{6}$	0	$-1/2\sqrt{6}$
$F=2$	$m_F=-1$	0	0	$-1/2\sqrt{2}$	0	$-1/2\sqrt{3}$	0	$1/2\sqrt{2}$	0
$F=2$	$m_F=-2$	0	0	0	$-1/2\sqrt{3}$	0	0	0	$1/2$
$F=1$	$m_F=1$	$-1/2$	0	$1/2\sqrt{6}$	0	0	0	$1/2\sqrt{6}$	0
$F=1$	$m_F=0$	0	$-1/2\sqrt{2}$	0	$1/2\sqrt{2}$	0	$1/2\sqrt{6}$	0	$1/2\sqrt{6}$
$F=1$	$m_F=-1$	0	0	$1/2\sqrt{6}$	0	$1/2$	0	$1/2\sqrt{6}$	0

Rahn [10]. A series of experimental spectra at increasing laser intensities were obtained for the 4WM and 8WM cases; unfortunately, such a series was not acquired for the 6WM case. For both experiment and theory, the polarization vector for the 4WM and 8WM signal was parallel to the polarization vector $\hat{\mathbf{e}}_2$, while the polarization vector for the calculated 6WM spectra was parallel to the polarization vector $\hat{\mathbf{e}}_1$. The intensities of the signals for the perpendicular polarizations ($\hat{\mathbf{e}}_1$ for the 4WM and 8WM and $\hat{\mathbf{e}}_2$ for the 6WM) were negligible because the medium is isotropic, and an even number of photons must be involved in the interaction from each polarization.

Experimental and calculated 4WM spectra are shown in Figs. 14 and 15, respectively. The calculated 4WM spectra are in good agreement with experiment. The asymmetry in the resonance at 0.059 cm^{-1}, with higher intensity in the wings on the high-frequency (more positive $|\omega_1-\omega_2|$) side, is reproduced in the calculated spectrum. As the laser intensity increases, the resonance at 0.059 cm^{-1} broadens and a noticeable dip appears near 0.03 cm^{-1}. A comparison of Figs. 14 and 15 shows that the model does a good job of predicting the development of the 4WM spectrum with increasing laser intensity. For experimental and theoretical spectra of similar shape in Figs. 14 and 15, the theoretical laser intensity (per laser beam) is a factor of 1.5 to 2 times higher than the experimental intensity [with the exception of Figs. 14(a) and 15(a), where the intensity is low enough that the line shape is independent of laser intensity]; we regard this as excellent agreement. It is interesting to note that in both experiment and the 16-level model, a peak appears at 0.03 cm^{-1} as laser intensity increases, whereas in the three-level model a dip appears (Fig. 5).

The theoretical intensity should be somewhat higher than the experimental intensity because we have assumed that two laser beams ($A_1=A_2$, $I_{L1}=I_{L2}$) are present in our calculations, whereas in the experiment three beams of equal intensity were used. However, there is also a factor-of-2 uncertainty in the electronic dephasing collision rate, which determines in large part the strength ("saturation intensity") of the wave-mixing interaction [10,17]. In addition, while we have assumed spatially perfect beams in our calculations, it is possible that any imperfections (hot spots) in the actual laser-beam profiles would have emphasized the wave-mixing processes because these processes depend on higher powers of laser intensity. For a comparison of theory and experiment, it is much more significant that the ratio of the experimental to theoretical laser intensity is approximately constant for Figs. 14(b)–14(d) and 15(b)–15(d).

The most noticeable difference between theory and experiment is that the theory predicts a more significant background contribution that appears to arise from the tail of the zero-frequency resonance. This resonance is discussed in detail by Rothberg and Bloembergen [17]

TABLE IV. Values of the collisional rates used in the 16-level model calculations. For the population transfer rates, it is assumed that collisional transfer to any given final state m is equally probable.

Coherence dephasing collision rates	
Ground-state coherences (k,m both ground states)	$\gamma_{km}=3.0\times10^8$ sec^{-1}
Excited-state coherences (p,s both excited states)	$\gamma_{ps}=3.0\times10^9$ sec^{-1}
Electronic resonance ($s=$ excited state, $m=$ ground state)	$\gamma_{sm}=5.0\times10^9$ sec^{-1}
Population transfer collision rates	
Ground states (k,m both ground states)	$\sum_m \Gamma_{km}=1.0\times10^6$ sec^{-1}
Excited states (p,s both excited states)	$\sum_s \Gamma_{ps}=1.0\times10^6$ sec^{-1}
Electronic transfer ($s=$ excited state, $m=$ ground state)	$\sum_m \Gamma_{sm}=1.0\times10^9$ sec^{-1}

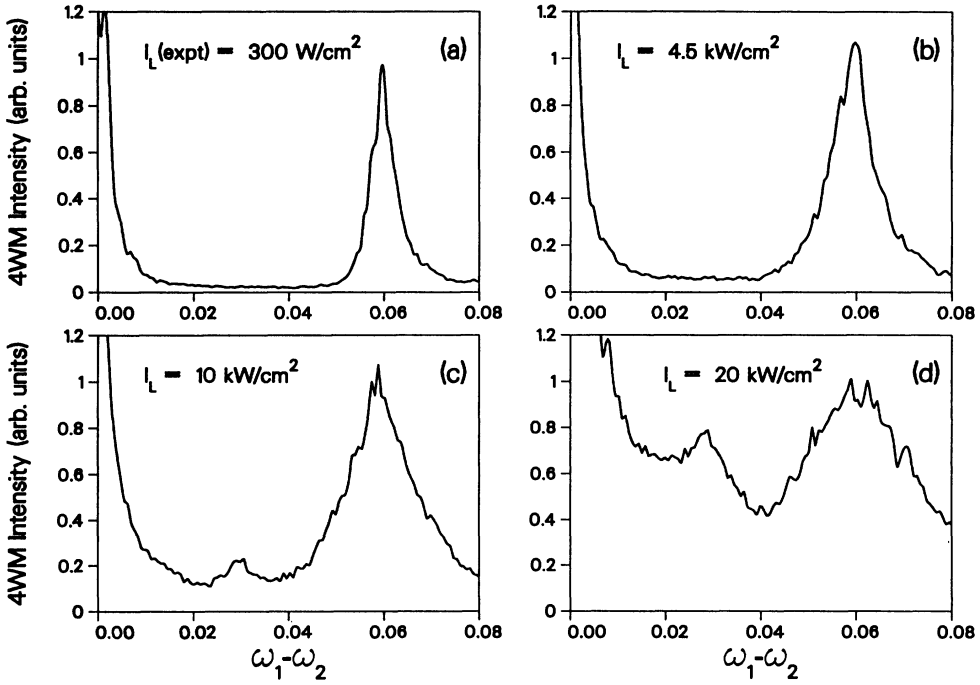

FIG. 14. Experimental 4WM spectra obtained by Trebino and Rahn [10] at four different laser intensities.

and modeled in a recent paper by Singh and Agarwal [41]; processes such as Doppler broadening and velocity narrowing that affect the line shape and intensity of this resonance have not been included in our calculation. Consequently, the difference in the background between theory and experiment is not surprising.

Good agreement is also obtained between experimental and calculated 8WM spectra. The best agreement is obtained at low intensity when the only noticeable spectral features are the first and second subharmonics at 0.03 and 0.02 cm^{-1}, respectively. The low-intensity 8WM spectra shown in Figs. 16 and 17 differ markedly from the

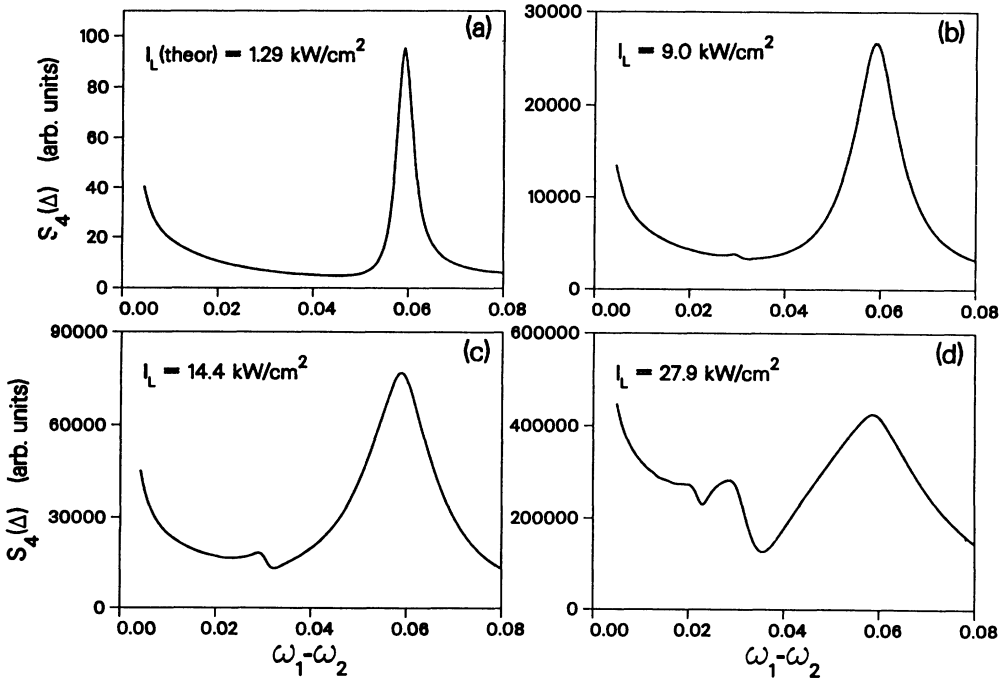

FIG. 15. Calculated 4WM spectra for the 16-level system.

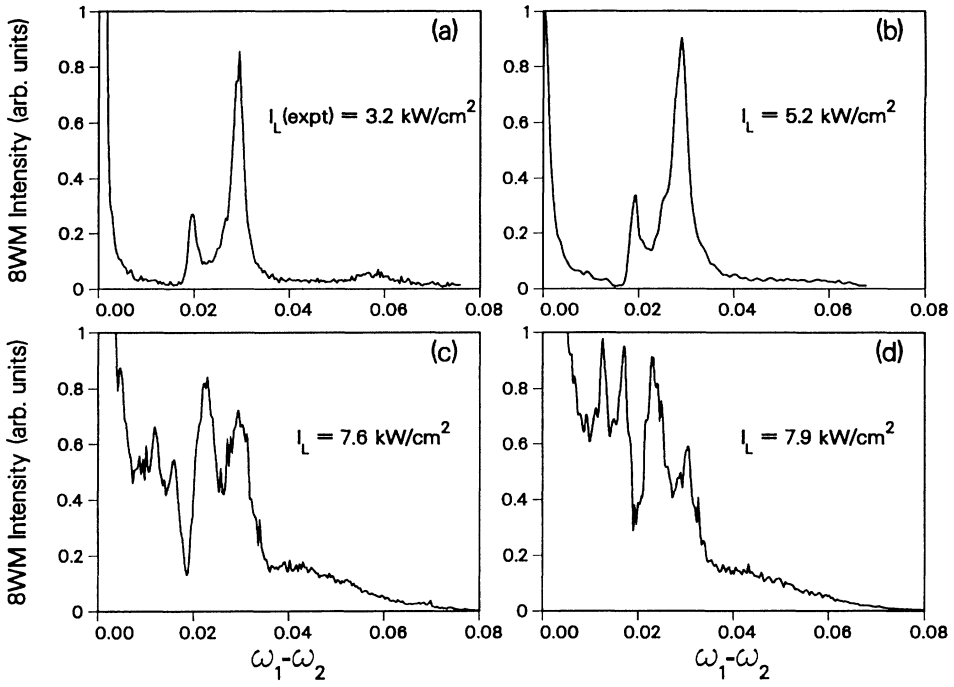

FIG. 16. Experimental 8WM spectra obtained by Treinbo and Rahn [10] at four different laser intensities.

low-intensity spectra for the three-level model shown in Fig. 7(a), where only the subharmonic at 0.02 cm^{-1} is apparent.

As laser intensity increases, the peaks of the spectral features shift to greater frequency difference, the third and fourth subharmonics at 0.015 and 0.012 cm^{-1} appear, and an additional spectral feature appears at approximately at 0.04 cm^{-1}. It is possible that this spectral feature at 0.04 cm^{-1} results from a splitting and appearance of a dip in the first subharmonic. Although at high intensity the tail of the zero-frequency resonance is underpredicted, all of the spectral features discussed above are present in the experimental as well as the calculated 8WM spectra. The theoretical laser intensity is a factor

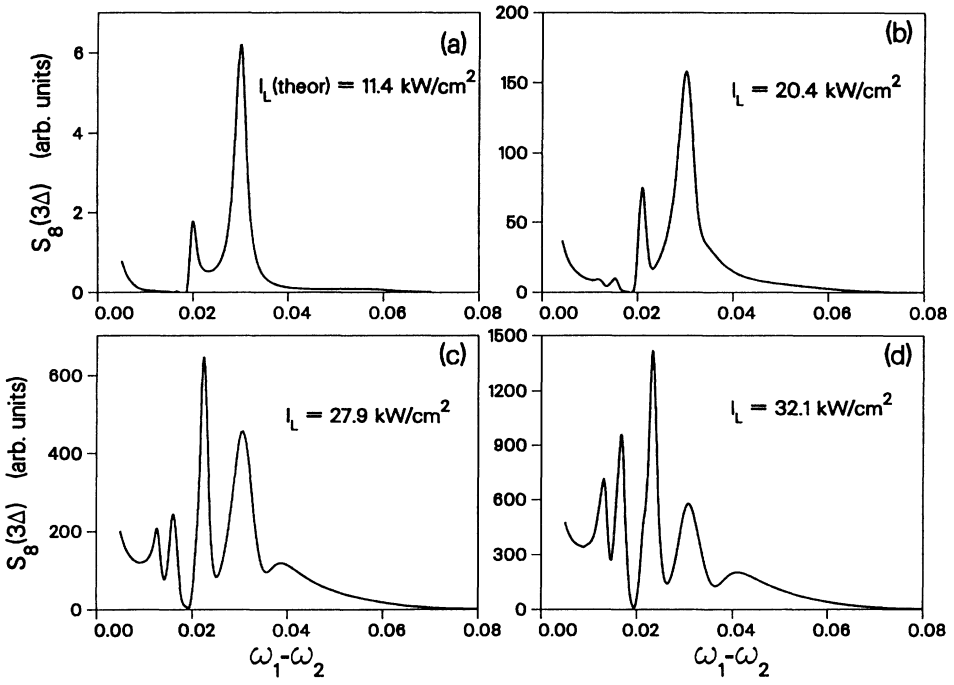

FIG. 17. Calculated 8WM spectra for the 16-level system.

of 3 to 4 times higher than the experimental intensity for the 8WM spectra shown in Figs. 16 and 17. However, the ratio of the theoretical to experimental intensity varies only between 3.6 and 4.1 for these spectra. Again, we regard the agreement between theoretical and experimental laser intensities to be excellent.

The agreement between theory and experiment becomes worse as the laser intensity increases because the relative intensities and frequency positions for the spectral features become very sensitive to laser intensity. The spatial intensity profile and pulse-to-pulse energy fluctuation of the laser radiation thus increase noise and broaden spectral features in the experimental spectra. The spatial intensity profile and pulse-to-pulse fluctuation of the laser are not included in the calculations, and the spectral features therefore tend to be narrower.

One feature of the 8WM spectrum that consistently differs between theory and experiment that cannot be explained by the characteristics of the laser radiation is the shoulder of the resonance at zero-frequency difference. It is much stronger for the experimental than calculated spectra at high intensity; this is the opposite of the case for 4WM, where the background contribution is higher in the theory than in the experiment. Once again, we feel that the disagreement between theory and experiment occurs because processes such as Doppler broadening and velocity narrowing are not included in our model.

Figure 18 shows calculated 8WM spectra at three laser intensities that are slightly higher than the laser intensity for the spectrum shown in Fig. 17(d). The spectrum shown in Fig. 18(b) has a pronounced dip at line center for the resonance feature at 0.25 cm^{-1}; a slight dip is also noticeable on the low-frequency side of this line in Fig. 18(a) and on the right side of the line in Fig. 18(c). Thus, as laser intensity increases, the dip in the resonance line appears to move to higher detuning frequency.

An experimental 6WM spectrum is shown in Fig. 19. Unlike the case for 4WM and 8WM, a series of spectra as a function of increasing laser intensity are not available. The calculated 6WM spectra shown in Fig. 20 are very interesting, however. In the low-intensity spectrum shown in Fig. 20(a), the dispersive character of the feature near 0.02 cm^{-1} suggests that an interference is occurring between a 6WM resonance and the tail of the zero-frequency resonance, or perhaps between different wave-mixing orders. This interference produces a pronounced dip in the spectrum at 0.02 cm^{-1} that is also present in the experimental spectrum. No such interferences are evident in the three-level model results (Fig. 6).

The similarity of the 6WM and 8WM spectra at high intensity should also be noted. For perpendicular laser-beam polarizations, 6WM resonances at $\omega_{hfs}/2$ are not allowed for the sodium $3\,^2S_{1/2}$–$3\,^2P_{1/2}$ electronic resonance. Instead, the 6WM resonances shown in Fig. 20 arise from higher-order $3\omega_1-2\omega_2+(\omega_1-\omega_1)$ or $3\omega_1-2\omega_2+(\omega_2-\omega_2)$ processes, i.e., eight or more photons are involved in the wave-mixing interaction. This will become more apparent when the intensity dependence of wave-mixing resonances is discussed in Sec. IV C.

As stated earlier in Sec. III A, for the same peak laser intensity, calculated spectra were nearly identical for unchirped 10- and 20-nsec pulses and chirped 20-ns pulses. This lack of dependence of the spectra on pulse length

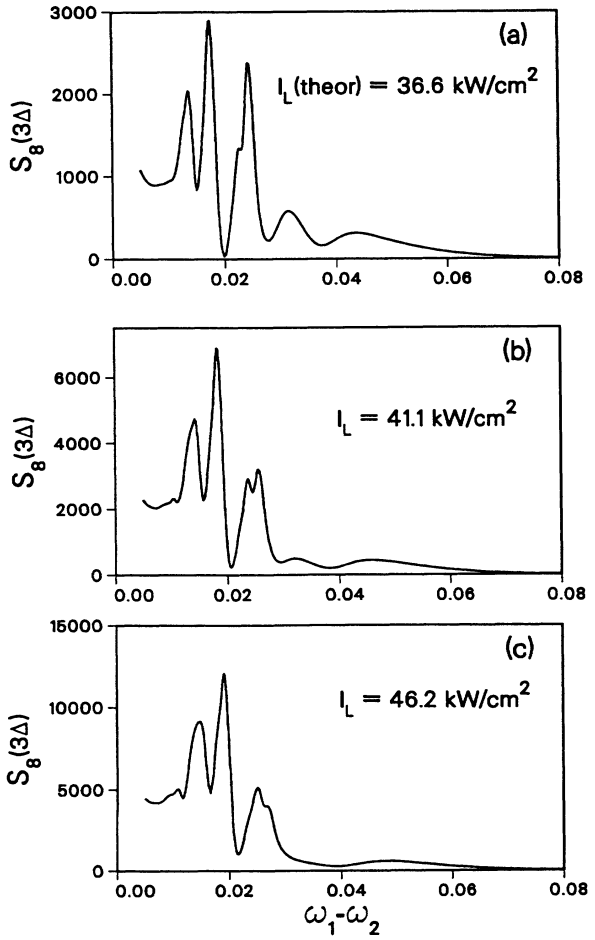

FIG. 18. Calculated 8WM spectra for the 16-level system at high laser power.

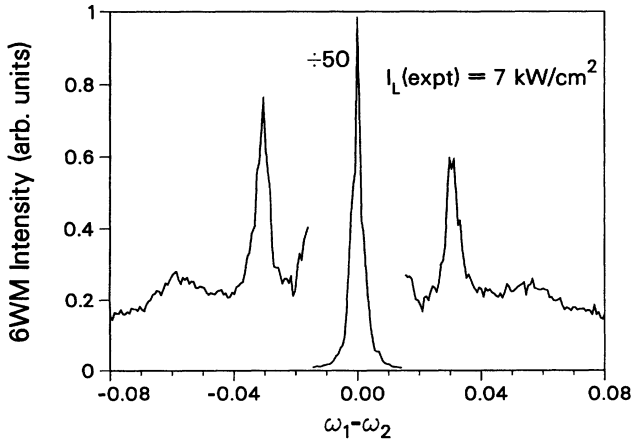

FIG. 19. Experimental 6WM spectra obtained by Trebino and Rahn [10].

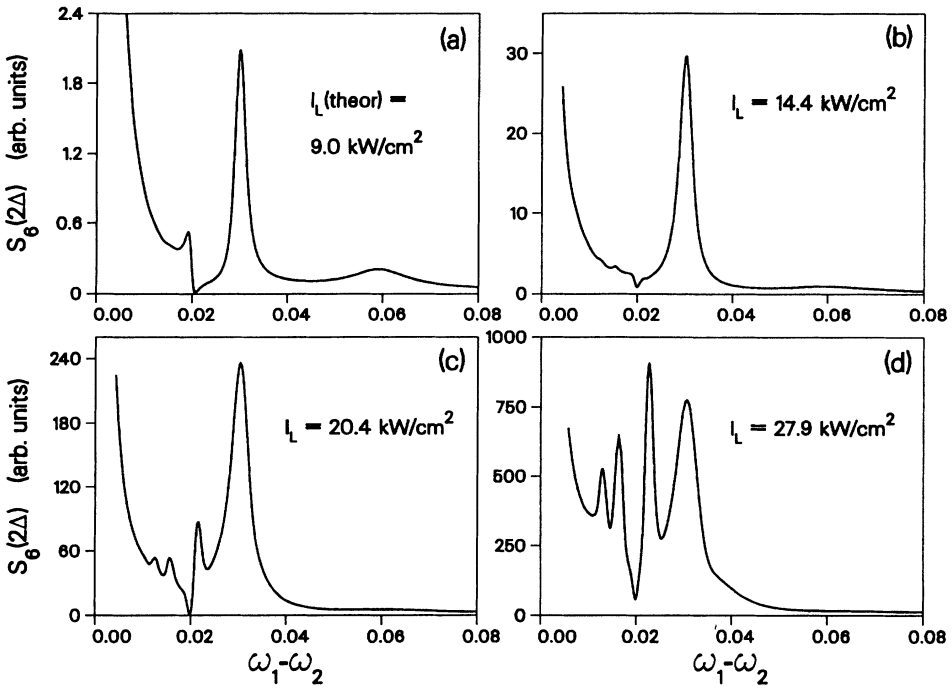

FIG. 20. Calculated 6WM spectra for the 16-level system.

and bandwidth implies that the laser frequency bandwidth is narrow enough to resolve fully the wave-mixing resonances. The lack of dependence on pulse length further implies that the pulses were long enough that the response of the 16-level system to the laser radiation reached steady state. This is not to imply that the density-matrix elements themselves became independent of time; they continue to show the same sort of oscillatory behavior shown in Figs. 10–13. Rather, the magnitudes of the various frequency components for the density-matrix elements probably reach steady-state values. This supposition can be studied by a detailed Fourier analysis of the density-matrix elements, but this has not yet been done.

Considerably more CPU time was required for the 16-level model calculations. Integration over a laser pulse to obtain a single point of the wave-mixing spectrum required 115 min of CPU time on the DEC station 3100, as compared to 4 min for the three-level system.

C. Laser-intensity dependence of the multiwave-mixing signals

In this section we discuss the intensity dependence of some of the spectral features in the calculated 4WM, 6WM, and 8WM spectra. The intensity dependence of these spectral features would be difficult to investigate experimentally with much accuracy because of the difficulty of measuring the required laser parameters and of maintaining stable enough laser operation to allow comparison of spectra collected at different times with different laser intensities. The laser-intensity dependence of the 4WM resonance at 0.059 cm^{-1} is shown in Fig. 21. The normalized 4WM signal $S_4(\Delta)/[I_L(\text{theor})]^3$ is plotted. As might be anticipated, the normalized intensity is very close to 1.0 for low laser intensity. As laser power increases, the resonance broadens and the normalized intensity decreases monotonically, i.e., the resonance exhibits its saturation behavior.

The laser-intensity dependence of the 6WM and 8WM resonances is very different. The normalized 6WM intensity $S_6(\Delta)/[I_L(\text{theor})]^5$ for the spectral feature at 0.03 cm^{-1}, shown in Fig. 22, first increases with laser intensity and reaches a maximum at

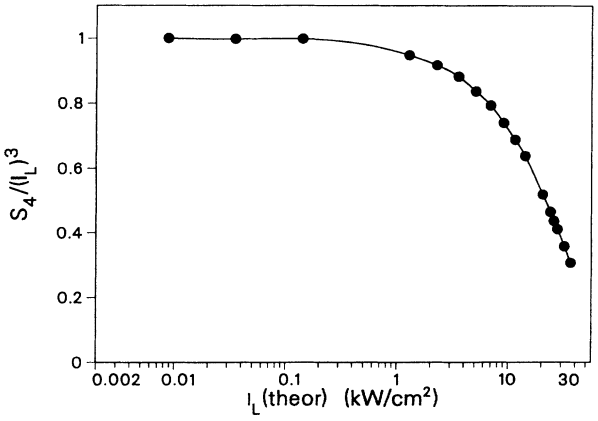

FIG. 21. Normalized 4WM intensity $S_4(\Delta)/(I_L)^3$ vs laser intensity. The normalized peak intensity of the resonance at 0.059 cm^{-1} (see Fig. 15) is plotted.

$I_L(\text{theor})=20$ kW/cm^2

before decreasing for higher laser intensity. The onset of the rapid increase in the normalized 6WM signal corresponds closely to the onset of significant population transfer in the 16-level system. According to the perturbation approach of Trebino and Rahn [20], the increase in the normalized 6WM intensity suggests that wave-mixing processes of order higher than 6 are contributing to the calculated 6WM signal. [For theoretical laser intensities below 1.7 kW/cm^2, the 6WM and 8WM signals cannot be separated reliably from background noise in the spectrum caused by residual noise in the Fourier integration. No points below $I_L(\text{theor})=2$ kW/cm^2 are plotted in Figs. 22 and 23.]

The laser-intensity dependence of the 8WM resonances at 0.02 and 0.03 cm^{-1} is shown in Fig. 23. The normalized signals $S_8(\Delta)/[I_L(\text{theor})]^7$ are at first fairly constant and then decrease significantly with increasing $I_L(\text{theor})$ for both of the resonances. This rapid decrease is somewhat surprising, although it corresponds to a region of rapid decrease in the normalized 4WM signal and indicates that perturbation theory is no longer valid. The rapid decrease in normalized 8WM intensity may be due to Stark shifting of the lines, which are rather narrow compared to 4WM or 6WM lines. It may be that the integrated intensity over the line would fall off less rapidly compared to the peak intensity plotted in Fig. 23. Because the resonances are overlapped and there is a potentially significant contribution from the shoulder of the zero-frequency Zeeman resonance, the integrated line intensity cannot be determined unambiguously. For the resonance at 0.02 cm^{-1}, the normalized signal is fairly constant between

$I_L(\text{theor})=15$ kW/cm^2

and

$I_L(\text{theor})=30$ kW/cm^2 .

The curve for the resonance at 0.03 cm^{-1} also exhibits a

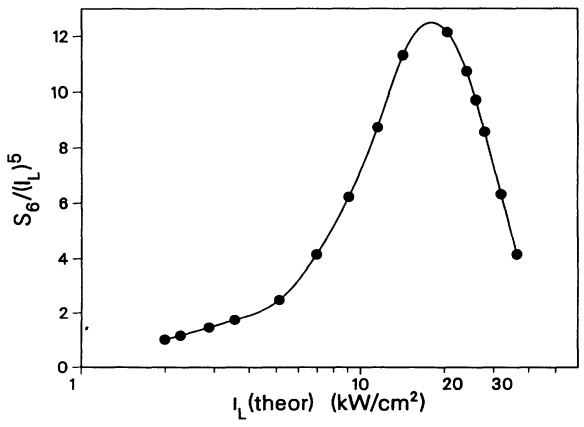

FIG. 22. Normalized 6WM intensity $S_6(2\Delta)/(I_L)^5$ vs laser intensity. The normalized peak intensity of the resonance at 0.03 cm^{-1} (see Fig. 20) is plotted.

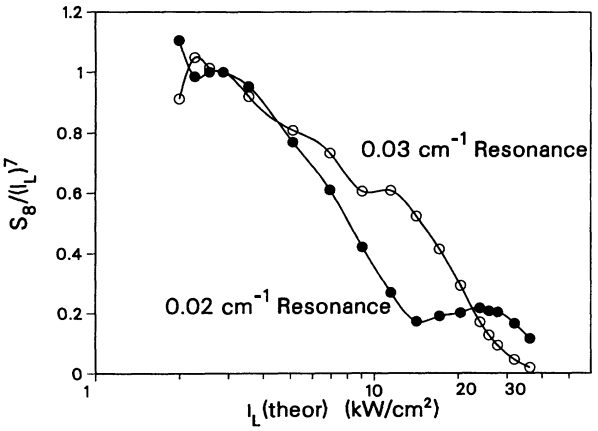

FIG. 23. Normalized 8WM intensity $S_8(3\Delta)/(I_L)^7$ vs laser intensity. The normalized peak intensities of the resonances at 0.02 and 0.03 cm^{-1} (see Fig. 17) are plotted. The peaks shift slightly with increasing laser intensity; the peak intensity for the resonance is plotted, rather than the signal intensity at 0.02 or 0.03 cm^{-1}.

brief flattening near

$I_L(\text{theor})=15$ kW/cm^2 .

These flat regions in the plot are evidence of the influence of wave-mixing processes of order 10 or higher.

V. CONCLUSIONS

Resonant multiwave mixing in a three-level system and in the gas-phase sodium atom pumped by two nearly degenerate laser beams was investigated theoretically. The $3\,^2S_{1/2}$–$3\,^2P_{1/2}$ electronic resonance of sodium was modeled as a 16-level system. The time development of the multilevel system was determined by numerical integration of the time-dependent density-matrix equations. Multiwave-mixing spectra were then determined directly from the calculated induced polarization. These calculations were validated by comparison with the experimental results of Trebino and Rahn [10].

This approach to modeling high-intensity wave-mixing interactions in atomic systems involved significantly fewer simplifying assumptions than previous high-intensity analysis [21–23]. The drawback of direct numerical integration of the density-matrix equations is that analytic solutions are not obtained, and physical insight into the wave-mixing processes can be gained only by detailed analysis of the numerical solutions. However, the development of a framework for direct numerical simulation of the excitation dynamics in a complicated multilevel system opens up new possibilities for the investigation of the physics of the interaction of laser radiation with atomic or molecular resonances. For example, the three-level system was used to study the close coupling between the population dynamics and the development of the induced polarization. We have also begun to explore the laser excitation dynamics of the 16-level system in detail, and plan to present the results in a future publication. As

another example, the laser power dependence of 4WM, 6WM, and 8WM signals was investigated theoretically for the 16-level system.

The numerical methods applied here are potentially applicable to a large number of problems such as electronic resonance CARS [42] and resonant DFWM [43–45]. DFWM calculations that are nonperturbative in all three beams would be of great interest. For the DFWM calculations, the density-matrix equations must be integrated in space as well as time. Inclusion of the Doppler effect in the calculations is another significant hurdle for realistic simulation of experimental spectra. The numerical methods discussed in this paper are not restricted to nearly degenerate laser beams. However, the laser frequencies must be within a few cm^{-1} of single-photon resonance to allow the calculations to be completed in a reasonable amount of time; the integration time step is inversely proportional to the frequency detuning.

There is great potential for significant decreases in CPU time required for these and similar calculations via massively parallel processing. The spectral calculations are almost trivially parallelizable. Each processor can integrate the density-matrix equations for a different value of laser detuning; the calculations for each value of $\omega_1-\omega_2$ are completely independent. Parallel processing would greatly expand the scope of the problems that could be addressed and the detail with which they could be addressed.

ACKNOWLEDGMENT

This work was supported by the U.S. Department of Energy, Office of Basic Energy Sciences, Division of Chemical Sciences.

[1] N. Bloembergen, *Nonlinear Optics* (Benjamin, Reading, MA, 1965).
[2] Y. R. Shen, *The Principles of Nonlinear Optics* (Wiley, New York, 1984), pp. 242–284.
[3] A. C. Eckbreth, *Laser Diagnostics for Combustion Temperature and Species* (Abacus Press, Cambridge, MA, 1988).
[4] S. P. Druet and J. P. E. Taran, Prog. Quantum Electron. **7**, 1 (1981).
[5] R. P. Lucht, R. E. Teets, R. M. Green, R. E. Palmer, and C. R. Ferguson, Combust. Sci. Technol. **55**, 41 (1987).
[6] P.-L. Zhang, Y.-C. Wang, and A. L. Schawlow, J. Opt. Soc. Am. B **1**, 9 (1984).
[7] P.-L. Zhang and A. L. Schawlow, Can. J. Phys. **62**, 1187 (1984).
[8] J. Reintjes, C.-Y. She, and R. C. Eckardt, IEEE J. Quantum Electron. **QE-14**, 581 (1978).
[9] R. K. Raj, Q. F. Gao, D. Bloch, and M. Ducloy, Opt. Commun. **51**, 117 (1984).
[10] R. Trebino and L. A. Rahn, Opt. Lett. **12**, 912 (1987).
[11] D. Debarre, M. Lefebvre, and M. Pealat, Opt. Commun. **69**, 362 (1989).
[12] L. Zheng, C. Wang, and Y. Wu, Opt. Commun. **59**, 293 (1986).
[13] A. McPherson, G. Gibson, H. Jara, U. Johann, T. S. Luk, I. A. McIntyre, K. Boyer, and C. K. Rhodes, J. Opt. Soc. Am. B **4**, 595 (1987).
[14] M. Ferray, A. L'Huiller, X. F. Li, L. A. Lompré, G. Mainfray, and C. Manus, J. Phys. B **21**, L31 (1988).
[15] K. C. Kulander and B. W. Shore, Phys. Rev. Lett. **62**, 524 (1989).
[16] J. H. Eberly, Q. Su, and J. Javanainen, Phys. Rev. Lett. **62**, 881 (1989).
[17] L. J. Rothberg and N. Bloembergen, Phys. Rev. A **30**, 820 (1984).
[18] G. S. Agarwal, Opt. Lett. **13**, 482 (1988).
[19] N. C. Kothari and G. S. Agarwal, Opt. Commun. **74**, 342 (1990).
[20] R. Trebino and L. A. Rahn, Opt. Lett. **15**, 354 (1990).
[21] A. M. Levine, N. Chencinski, W. M. Schreiber, A. N. Weiszmann, and Y. Prior, Phys. Rev. A **35**, 2550 (1987).
[22] N. Chencinski, W. M. Schreiber, A. M. Levine, and Y. Prior, Phys. Rev. A **42**, 2839 (1990).
[23] B. Dick and R. M. Hochstrasser, Chem. Phys. **75**, 133 (1983).
[24] A. D. Wilson-Gordon and H. Friedmann, Phys. Rev. A **38**, 4087 (1988).
[25] G. S. Agarwal, Phys. Rev. A **43**, 1523 (1991).
[26] F. A. M. Oliveira, C. B. de Araújo, A. S. L. Gomes, and L. H. Acioli, Phys. Rev. A **43**, 3724 (1991).
[27] R. P. Lucht and R. L. Farrow, J. Opt. Soc. Am. B **5**, 1243 (1988).
[28] R. P. Lucht and R. L. Farrow, J. Opt. Soc. Am. B **6**, 2313 (1989).
[29] D. P. Weitekamp, K. Duppen, and D. Wiersma, Phys. Rev. A **27**, 3089 (1983).
[30] F. Kannari and M. Obara, J. Opt. Soc. Am. B **7**, 1493 (1990).
[31] B. W. Shore, *The Theory of Coherent Atomic Excitation* (Wiley, New York, 1990), Vols. 1 and 2.
[32] S. Stenholm, *Foundations of Laser Spectroscopy* (Wiley, New York, 1984).
[33] M. D. Levenson, *Introduction to Nonlinear Laser Spectroscopy* (Academic, New York, 1982).
[34] A. E. Siegman, *Lasers* (University Science Books, Mill Valley, CA, 1986).
[35] B. J. Dalton and P. L. Knight, Opt. Commun. **42**, 411 (1982).
[36] P. M. Radmore, Phys. Rev. A **26**, 2252 (1982).
[37] Ya. I. Khanin and O. A. Kocharoskaya, J. Opt. Soc. Am. B **7**, 2016 (1990).
[38] L. I. Schiff, *Quantum Mechanics* (McGraw-Hill, New York, 1968).
[39] J. T. Fourkas, T. R. Brewer, H. Kim, and M. D. Fayer, Opt. Lett. **16**, 177 (1991).

[40] J. E. M. Goldsmith, Opt. Lett. **6**, 525 (1981).
[41] S. Singh and G. S. Agarwal, Phys. Rev. A **42**, 3070 (1990).
[42] B. Attal-Trétout, S. C. Schmidt, E. Crété, P. Dumas, and J. P. Taran, J. Quant. Spectrosc. Radiat. Transfer **43**, 351 (1990).
[43] P. Ewart and S. V. O'Leary, Opt. Lett. **11**, 279 (1986).
[44] T. Dreier and D. J. Rakestraw, Opt. Lett. **15**, 72 (1990).
[45] T. Dreier and D. J. Rakestraw, Appl. Phys. B **50**, 479 (1990).

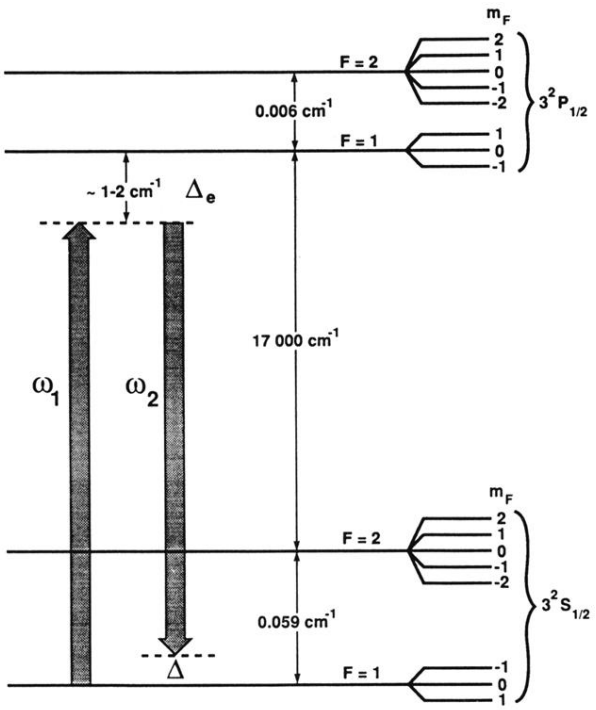

FIG. 1. Energy-level diagram for multiwave mixing in the sodium $3\,^2S_{1/2}$–$3\,^2P_{1/2}$ electronic system.

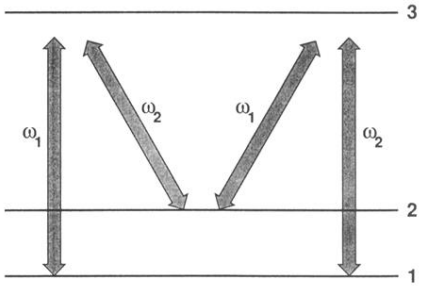

FIG. 3. Schematic diagram of the M-type system.

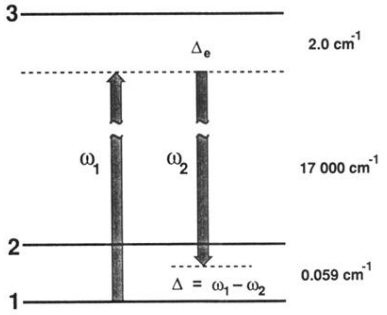

FIG. 4. Energy-level diagram for the three-level system.

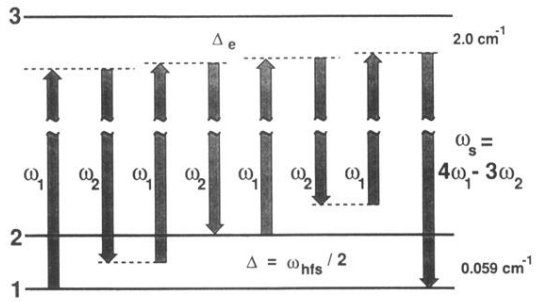

FIG. 8. Energy-level diagram for eight-wave mixing in the three-level system for a laser detuning $\omega_1 - \omega_2 = \omega_{hfs}/2$.

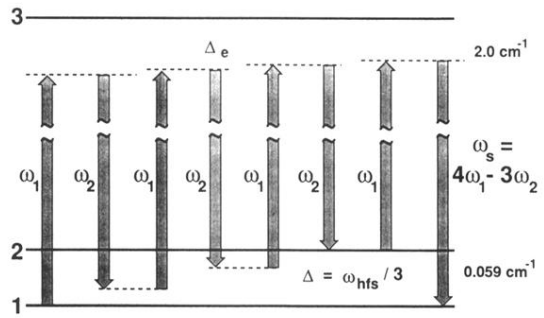

FIG. 9. Energy-level diagram for eight-wave mixing in the three-level system for a laser detuning $\omega_1 - \omega_2 = \omega_{hfs}/3$.